269 (2027) 214877

Contents lists available at ScienceDirect

Geoenergy Science and Engineering

journal homepage: www.sciencedirect.com/journal/geoenergy-science-and-engineering

Numerical simulation of single-well and dual-well systems of CO_2 hydrate-based sequestration in the South China Sea based on thermal–hydraulic–mechanical–chemical modeling

Hui Yang [a], Shuanshi Fan [a,b], Xuemei Lang [a,b], Chenlu Xu [c], Yanhong Wang [a,b,*], Mengyang Li [d]

[a] South China University of Technology, Guangzhou, 510640, China
[b] Key Laboratory of Heat and Mass Transfer and Low-Carbon Conversion, Ministry of Education, South China University of Technology, Guangzhou, 510640, China
[c] National Engineering Research Center of Gas Hydrate Exploration and Development, Guangzhou Marine Geological Survey, China Geological Survey, Guangzhou, 511458, China
[d] College of Electromechanical Engineering, Qingdao University of Science and Technology, Qingdao, 266061, China

ARTICLE INFO

Keywords:
CO_2 hydrate
Carbon sequestration
Numerical simulation
Thermal–hydraulic–mechanical–chemical model
Dual-well system

ABSTRACT

CO_2 hydrate sequestration technology enables large-scale carbon storage by forming solid hydrates in marine sediments, offering a promising approach to mitigating global climate change. However, storing substantial volumes of CO_2 as hydrates can induce considerable stress redistribution and formation deformation, which may compromise sub-seafloor infrastructure and potentially trigger geohazards such as submarine landslides. Existing experimental and numerical studies have primarily focused on CO_2 migration, hydrate formation, and storage performance, while comparatively limited attention has been paid to the mechanical behavior of hydrate-bearing sediments and its impact on CO_2 storage performance. Therefore, in this study, mechanical parameters were introduced to develop a thermal–hydraulic–mechanical–chemical (THMC) model to simulate CO_2 hydrate sequestration. The mechanical behavior of the sediments was described using an elastoplastic constitutive model based on the Mohr–Coulomb yield criterion. The model was validated against laboratory-scale CO_2 hydrate formation experiments, showing good agreement with the experimental results, with a calculated error of 10.18%. The model was applied to analyze CO_2 storage in South China Sea reservoirs. By comprehensively accounting for mechanical effects, we evaluated CO_2 sequestration performance and reservoir stability, and further compared storage potential between single-well and dual-well systems. The results indicate that in the single-well system, effective stress decreased rapidly after CO_2 injection, causing seabed uplift of approximately 0.2 m. Over long-term storage, the principal effective stress did not evolve toward yield failure, suggesting system stability under prolonged operation. Compared with the THMC model, the THC model predicted smaller reductions in porosity and permeability because sediment deformation was not considered, and the storage capacity increased from 8.69×10^6 kg to 8.82×10^6 kg, leading to an overestimation of the predicted CO_2 storage. In the dual-well system, the combined effects of heat and mass transfer and multiphase flow significantly improved the storage performance, increasing the total stored amount by 2.48 times compared with the single-well system. Overall, mechanical coupling is important for evaluating reservoir deformation and storage safety, while the dual-well configuration significantly improves CO_2 storage efficiency.

1. Introduction

Carbon dioxide (CO_2), a major greenhouse gas, is a key contributor to global warming and climate change. Controlling and reducing CO_2 emissions has therefore become a critical global priority (Allen et al., 2009; Hepburn et al., 2019). Under the low-temperature, high-pressure conditions of marine sediments, CO_2 can react with water to form solid hydrates, offering a potential mechanism for sequestration. In particular, storing CO_2 as hydrates in marine sediments is considered a safe and technically viable long-term carbon storage strategy (Zheng et al., 2020; Pandey et al., 2022; Wang et al., 2024a). Notably, one volume of CO_2 hydrate can trap approximately

* Corresponding author. South China University of Technology, Guangzhou, 510640, China.
E-mail address: wyh@scut.edu.cn (Y. Wang).

https://doi.org/10.1016/j.geoen.2026.214877
Received 26 December 2025; Received in revised form 19 September 2026; Accepted 16 October 2026
Available online 27 October 2026
2949-8910/© 2026 Published by Elsevier B.V.

160–184 vol of CO_2 gas (Dhamu et al., 2023). Geographically, CO_2 hydrates typically form in shallow sub-seabed sediments, where they can act as a low-permeability caprock. This sealing effect restricts the upward migration of stored CO_2 and significantly lowers the risk of leakage, which is a major concern in carbon storage systems (Rehman et al., 2021; Zhao et al., 2022). Recent studies have further emphasized that thermodynamic conditions and multiphase flow characteristics, such as temperature effects and relative permeability hysteresis, play crucial roles in controlling CO_2 dissolution, migration, and trapping behavior in saline aquifers(Salaudeen et al., 2026; Juanes et al., 2006). These findings provide important insights into CO_2 transport mechanisms relevant to subsurface storage systems. Due to these advantages, hydrate-based CO_2 sequestration has gained considerable research interest in the field of marine carbon storage (Aminnaji et al., 2024; Sinehbaghizadeh et al., 2022; Yang et al., 2024).

As early as 1997, Koide et al. (1997) first proposed the concept of CO_2 sequestration in geological formations via hydrate formation, and they further investigated the conditions required for CO_2 hydrate formation under specific temperature regimes and ocean depth ranges. Through numerical simulations, Teng and Zhang (2018) identified deep-sea regions where CO_2 hydrates exhibit negative buoyancy. In these regions, both liquid CO_2 and CO_2 hydrates possess densities greater than that of seawater. This density difference facilitates the formation of a stable hydrate layer, which acts as a physical barrier to impede upward CO_2 migration, thereby effectively reducing leakage risk. The feasibility of this sequestration method was experimentally validated by Qureshi et al. (Fahed Qureshi et al., 2022) using a laboratory-scale high-pressure reactor simulating marine sediment conditions. Their experiments demonstrated that CO_2 hydrates remained stable on the reactor's inner wall and within a sand pack for one month, providing direct evidence for the long-term stability of hydrate-based CO_2 storage.

The CO_2 hydrate sequestration process involves coupled thermal, hydraulic, mechanical,and chemical (THMC) interactions, encompassing hydrate formation kinetics, heat transfer during phase transitions, fluid flow in porous media, and geomechanical deformation induced by hydrate formation (Teng and Zhang, 2018; Li et al., 2025a). Compared to field studies, numerical simulation is an essential tool for evaluating CO_2 storage potential, offering strong predictive capability, flexibility, and cost-effectiveness (Inoue et al., 1996; Xia et al., 2024; Zhang et al., 2024; Bahmaee et al., 2024). Liu et al. (2023) developed a thermal–hydraulic–chemical (THC) model using the CMG-STARS simulator to analyze CO_2 hydrate storage in deep-sea sediments of the South China Sea, assessing the impact of key parameters on hydrate distribution and storage capacity. Gu et al. (2025) established a THC-coupled numerical program to simulate liquid CO_2 injection and subsequent hydrate formation in silty sediments of the same region. And they tracked the migration of liquid CO_2 and the spatiotemporal evolution of CO_2 hydrate, liquid CO_2, and dissolved CO_2 over a 5-year injection period followed by 100 years of storage. Xia et al. (2025) constructed a THC numerical model for CO_2 sequestration in mixed muddy–sandy settings and compared single- and dual-horizontal well configurations. Their results showed that higher injection rates accelerate hydrate cap formation but reduce storage efficiency, while lower rates prolong injection time, moderate pressure buildup, and enlarge cap coverage. In dual-well systems, closer spacing was found to promote broader hydrate cap development. Li et al. (2025b) developed a three-field THC-coupled numerical model to simulate CO_2 hydrate cap formation in sandy siltstone formations of the South China Sea, investigating the influence of formation and injection parameters on storage capacity and leakage risk. The simulation results indicated that positioning the injection well higher within the formation generates a wider lateral hydrate cap but also expands the potential leakage range of liquid CO_2.

While previous studies have mainly focused on CO_2 migration, hydrate formation, and storage performance, comparatively limited attention has been paid to the coupled mechanical response of hydrate-bearing sediments and its impact on CO_2 sequestration. Changes in pore pressure and hydrate formation may induce stress redistribution and reservoir deformation, thereby affecting reservoir properties and storage performance. Therefore, incorporating geomechanical effects is essential for evaluating the long-term safety and stability of CO_2 hydrate sequestration. Wang et al. (2024b) employed low-field nuclear magnetic resonance (NMR) to study hydrate distribution and structural changes in sediments with two representative clays. Their findings indicate that clay minerals accelerate CO_2 hydrate dissociation, disrupt initial water distribution, and alter pore architecture. Phase transitions during hydrate formation can induce irreversible deformation of the sediment skeleton, while pore blockage ultimately reduced CO_2 storage capacity. However, current models typically treat sediments as idealized elastoplastic media, neglecting the impacts of phase-change-induced volume variation and pore restructuring on fluid flow and heat transfer. Consequently, these models fail to accurately capture stress evolution and structural modification. This limited understanding of the mechanical response of the reservoir during CO_2 sequestration hinders reliable assessment of storage safety. The long-term stability of CO_2 in marine sediments depends not only on physical trapping by hydrates but is also synergistically driven by residual, dissolution, and mineral trapping mechanisms. Wettability and nanoparticle treatments can significantly alter rock dissolution rates and the associated risks of CO_2 leakage (Khoramian et al., 2025a). Moreover, such oversimplification of mechanical behavior compromises the credibility of simulation results and reduces the accuracy of long-term storage predictions.

COMSOL Multiphysics is a finite element method–based platform designed for solving partial differential equations (PDEs), and has demonstrated strong capability in accurately simulating large-scale hydrate exploitation and carbon sequestration processes (Wei et al., 2022; Yin et al., 2022a). Its distinct advantages in mechanical field simulation make it particularly suitable for this study compared to other numerical simulators (Jafari et al., 2023; Sarkar et al., 2022). Here, we used COMSOL to develop a fully coupled thermal–hydraulic–mechanical–chemical (THMC) model for CO_2 hydrate sequestration, explicitly integrating reservoir mechanical deformation with other physical fields. The model was applied to investigate the feedback of formation deformation on CO_2 migration and storage performance. Additionally, a dual vertical well configuration was modeled to enhance CO_2 hydrate storage efficiency, and the interaction mechanisms between single-well and dual-well systems were comparatively investigated. This work provides mechanistic insights into the effects of geomechanical deformation and inter-well interactions on CO_2 hydrate–based sequestration in marine sediments.

2. Model

2.1. Governing equations

The injection of CO_2 into subsea reservoirs and its subsequent hydrate formation constitute a multiphysics-coupled process that encompasses hydrate formation kinetics, multiphase flow of CO_2 and water, heat transfer and convection, and reservoir geomechanical deformation. A fully coupled thermal–hydraulic–mechanical–chemical (THMC) model was developed using COMSOL Multiphysics to simulate CO_2 hydrate sequestration in the South China Sea. The mathematical model describing the multiphase, multicomponent THMC processes during CO_2 storage was established based on the following assumptions:

(1) The mathematical model includes three phases (liquid CO_2, water, and hydrate) and three components (CO_2, water, and hydrate). CO_2 dissolution in the aqueous phase is not explicitly modeled as an independent dissolved-CO_2 component. The flow of the CO_2 phase and the water phase follows Darcy's law, while the hydrate phase is assumed to be stationary.

(2) After CO_2 injected into the reservoir, it quickly reaches a local thermal equilibrium state.
(3) The effect of salinity of pore water on hydrate phase equilibrium is neglected to simplify the THMC formulation and focus on the coupled thermal, hydraulic, mechanical, and chemical processes (Jeenmuang et al., 2024).
(4) The hydrate and sediment particles form a continuous solid skeleton that jointly bears the load of the hydrate reservoir, and their relative movement can be neglected (Wan et al., 2018).
(5) Small-strain and small-displacement conditions are assumed during CO_2 injection and hydrate formation. The sediments are described using a Mohr–Coulomb elastoplastic constitutive model, with plastic yielding occurring only when the local stress state reaches the yield surface.
(6) The formation was assumed to be homogeneous to isolate the coupled effects of sediment deformation and injection-well configurations.

The governing equations used in the model include the mass conservation equation, the hydrate formation kinetics equation, the energy conservation equation, and the mechanical equilibrium equation. The mass conservation for each component can be expressed as:

$$\frac{\partial}{\partial t}(\phi\rho_C S_C) + \nabla(\rho_C v_C) = m_C \tag{1}$$

$$\frac{\partial}{\partial t}(\phi\rho_L S_L) + \nabla(\rho_L v_L) = m_L \tag{2}$$

$$\frac{\partial}{\partial t}(\phi\rho_H S_H) = m_H \tag{3}$$

The subscripts C, L, and H represent the CO_2, water, and hydrate phases, respectively; ϕ is the reservoir porosity, which is dimensionless; ρ_i is the density of each phase., kg/m^3; S_i is the saturation of each phase, which is dimensionless; v_i is the velocity of each fluid phase, m/s; m_i is the mass source caused by hydrate formation, $kg/(m^3 \cdot s)$.

The fluid velocity in porous media is described using Darcy's law:

$$v_C = -K\frac{k_{rC}}{\mu_C}(\nabla P_C + \rho_C g) \tag{4}$$

$$v_L = -K\frac{k_{rL}}{\mu_L}(\nabla P_L + \rho_L g) \tag{5}$$

In the equation, K is the absolute permeability of the reservoir, mD; k_{rC} andk_{rL} are the relative permeabilities of the fluids in the reservoir and are dimensionless; μ_i is the viscosity of each phase, $Pa\cdot s$; P_i is the pressure of each phase,MPa.

The formation of CO_2 hydrates can be described by the following reaction:

$$CO_2(l) + nH_2O(l) \leftrightarrow CO_2 \cdot nH_2O(s) \pm heat \tag{6}$$

here, n represents the hydration number, which is taken as 6 in this study(Anderson, 2003).

A modified Kim–Bishnoi model (Singh et al., 2020) is used to describe the kinetics of hydrate formation.

$$m_H = k_f \exp\left(-\frac{\Delta E}{RT}\right)\left(\phi A_{SH} S_L + \phi^2 A_{SH} S_L S_H\right)(P_C - P_e)M_H \tag{7}$$

The formation of hydrates consumes water and CO_2, and their consumption rates are calculated based on the hydrate formation rate and the stoichiometric relationship:

$$m_L = -m_H\frac{nM_L}{M_H}, m_C = -m_H\frac{M_C}{M_H} \tag{8}$$

In the equation, k_f is the kinetic constant for hydrate formation, $mol/(m^2 \cdot Pa \cdot s)$; ΔE is the activation energy of the reaction, J/mol; A_{SH} is the specific surface area of the hydrate, $1/m$; P_e is the phase equilibrium pressure at a given temperature, MPa; M_H, M_L andM_C represent the molar masses of hydrate, water, and CO_2, respectively, kg/mol. The equation representing the phase equilibrium of CO_2 hydrates (Rochelle et al., 2009) is as follows:

$$P_e = \exp\left(A - \frac{B}{T}\right) \tag{9}$$

here, A and B are the regression coefficients for phase equilibrium, and T is the temperature, K.

The formation of CO_2 hydrates releases energy to the surroundings, causing an increase in temperature. At the same time, the temperature rise alters the physical and mechanical properties of the fluids and increases their flow velocity. During the formation process, heat transfer mainly occurs in three forms: heat conduction, heat convection, and heat radiation. Heat radiation only occurs when the temperature exceeds 400 °C, which is not applicable to the subsea environment and can therefore be neglected. Thus, in this analysis, only heat conduction and heat convection are considered in the heat transfer process. By taking temperature T as the dependent variable in the heat transfer process, the energy conservation equation for hydrate-bearing sediments can be expressed as follows (Zhou et al., 2020):

$$\left[(1-\phi)\rho_s C_{p,s} + \phi\left(S_H\rho_H C_{p,H} + S_C\rho_C C_{p,C} + S_L\rho_L C_{p,L}\right)\right]\frac{\partial T}{\partial t} - \nabla\cdot(\lambda\nabla T) + \nabla\left[\left(\rho_C C_{p,C} v_C \phi S_C + \rho_L C_{p,L} v_L \phi S_L\right)T\right] = Q \tag{10}$$

In the equation, λ is the effective thermal conductivity, $\lambda = (1-\phi)\lambda_s + \phi(S_H\lambda_H + S_L\lambda_L + S_C\lambda_C)$,The subscript s denotes the rock skeleton; λ_H, λ_L, λ_C and λ_s represent the thermal conductivities of hydrate, water, CO_2, and the rock skeleton, respectively, $W/(m\cdot K)$. $C_{p,H}$, $C_{p,L}$, $C_{p,C}$ and $C_{p,s}$ represent the specific heat capacities of hydrate, water, CO_2, and the rock skeleton, respectively, $J/(kg\cdot K)$; Q is the heat source, W/m^3.

Because a subsea reservoir is a porous medium, the CO_2 and water in the pores are supported by a rock skeleton made of mineral grains and hydrates. According to Terzaghi's principle of effective stress, the static equilibrium equation for a hydrate reservoir that accounts for the effect of pore fluids can be written as (Sun et al., 2018):

$$\nabla\cdot\left(\sigma' + \alpha_B P_p \delta\right) - \sum_i (n_i\rho_i)g = 0, i = (L, C, H, s) \tag{11}$$

In the equation, σ' represents the effective stress, MPa; δ is a unit (identity) matrix; n_i is the volume fraction of each component; α_B is the Biot–Willis coefficient, which is taken as 1 in this study; P_p is the equivalent pore pressure of the fluid, in units of MPa, and can be calculated using the following equation:

$$P_p = \frac{P_C S_C + P_L S_L}{S_C + S_L} \tag{12}$$

Based on the basic principles and assumptions of small deformations in solid mechanics, the differential relationship between strain and displacement in the geometric equation is as follows(Wang et al., 2023a):

$$\varepsilon_{ij} = \frac{1}{2}\left(u_{i,j} + u_{j,i}\right) \tag{13}$$

Here, ε_{ij} is the displacement tensor, ; $u_{i,j}$ and $u_{j,i}$ are the displacement components, m.

During CO_2 injection and hydrate formation, changes in pore pressure and hydrate distribution can induce stress redistribution and deformation of the reservoir skeleton. The mechanical response is described using a small-strain elastoplastic constitutive model (Cheng et al., 2013):

$$d\sigma_{ij} = D_{ijkl} d\varepsilon_{kl} \tag{14}$$

In the equation, $d\sigma_{ij}$ is the increment of effective stress; D_{ijkl} is the elastoplastic coefficient matrix tensor; $d\varepsilon_{kl}$ is the increment of strain.

The elastoplastic behavior is governed by the Mohr-Coulomb yield criterion, which is suitable for describing the shear failure of hydrate-bearing sediments. Based on the representation in the principal stress space, the failure envelope can be expressed as a linear relationship between the maximum and minimum principal stresses:

$$\sigma_1 = \sigma_3 \cdot \frac{1 + \sin\varphi}{1 - \sin\varphi} + \frac{2c\cos\varphi}{1 - \sin\varphi} \tag{15}$$

Where σ_1 and σ_3 are the maximum and minimum principal stresses, respectively, φ is the internal friction angle, and c is the cohesion. In the numerical simulation, when the local stress state satisfies this failure criterion, the sediment is considered to undergo plastic yielding, which in turn affects reservoir stability and flow characteristics.

The evolution of plastic strain is described by a non-associated flow rule:

$$d\varepsilon_{ij}^{p} = d\lambda \frac{\partial g}{\partial \sigma_{ij}} \tag{16}$$

Where $d\lambda$ is the plastic multiplier, and g is the plastic potential function. The plastic potential is defined as:

$$g = \tau - \sigma_n \tan\psi \tag{17}$$

Where τ is the shear stress and σ_n is the normal stress, and ψ is the dilation angle controlling volumetric plastic deformation.

The elastoplastic constitutive model is implemented in COMSOL using the Solid Mechanics module. The Mohr–Coulomb model is adopted to describe the yield behavior of the reservoir. The material parameters required for the elastoplastic model are summarized in Table 1.

The THMC coupled model includes the formation of CO_2 hydrates from CO_2 and water, two-phase flow of water and CO_2 in the reservoir pores, heat release during hydrate formation, heat conduction and convection driven by two-phase flow, and mechanical deformation of the reservoir sediments. The mechanical field is coupled with the thermal, hydraulic, and chemical fields through changes in pore pressure and hydrate saturation. Pore-pressure variations affect the effective stress and induce sediment deformation, while the resulting deformation alters reservoir porosity and permeability, thereby feeding back to fluid flow, heat transfer, and hydrate formation. The coupling between the phase change (chemical field C), fluid flow (hydraulic field H), temperature field (T), and mechanical field (M) is realized through a series of cross-interaction terms expressed in the form of governing equations. COMSOL Multiphysics can robustly solve different types of partial differential equations, allowing for the numerical solution of these governing equations.

2.2. Model domain, boundary conditions, and initial conditions

This study was based on the geological conditions of the Shenhu area in South China Sea, with the reservoir model located below a water depth of 1500 m and a model domain of a 200 m square. The model was divided into a hydrate formation zone and an underlying rock layer. The thickness of hydrate formation zone was 150 m, and the underlying rock layer, located beneath the hydrate zone, had a thickness of 50 m. The reservoir was modeled as a two-dimensional Cartesian vertical cross-section with a fixed out-of-plane thickness of 200 m. The vertical well was represented as a narrow wellbore along the y-direction in the 2D cross-section, with the wellhead positioned in the underlying rock layer (y = −160 m) and a well radius of 0.1 m (Fig. 1a). Liquid CO_2 was injected into the reservoir through this vertical well at a constant total rate of 0.05 kg/s (4320 kg/d), with an initial injection temperature of 282.15 K. The reservoir model was discretized using a free triangular mesh. Considering the strong heat and mass transfer near the wellhead, the mesh around the wellhead was refined (Fig. 1b). The total number of mesh elements was 40582, with an average element quality of 0.938. During CO_2 injection and hydrate formation, the temperature and pressure at the boundaries around the model domain were assumed to remain constant. The bottom and side boundaries of the model fixed in the normal direction, while the top boundary beared the seawater load, was assumed to be free to move.

Under initial conditions, the pressure throughout the reservoir was influenced by the hydrostatic pressure distribution. The pressure at the top of the hydrate formation zone was approximately 15.3 MPa. The initial temperature field of the reservoir followed a geothermal gradient of 0.03 °C/m, with the top of the natural gas hydrate layer at an initial temperature of 3 °C. The initial porosity of the reservoir was 0.32, and the entire reservoir was fully saturated with water under the initial conditions. The basic parameters used in the simulation listed in Table 2.

It should be noted that the current model assumes a homogeneous formation to isolate and clarify the fundamental THMC coupling mechanisms during CO_2 injection. However, real marine sediments, such as those in the Shenhu area of the South China Sea, exhibit pronounced geological heterogeneity. Variations in permeability, porosity, and pore structure may significantly influence CO_2 migration pathways and hydrate distribution. In heterogeneous systems, preferential flow channels may develop, leading to uneven CO_2 accumulation and spatially variable hydrate formation. Such heterogeneity may also affect local pressure and temperature fields, thereby influencing hydrate stability. In addition, different flow regimes induced by geological heterogeneity can alter CO_2 trapping efficiency and dissolution behavior (Khoramian et al., 2026a). Therefore, while the current model captures the fundamental mechanisms of CO_2 migration and hydrate-based sealing, incorporating geological heterogeneity is essential for more realistic predictions.

Table 1
Mechanical parameter settings.

Parameter	Value	Parameter	Value
Cohesion c (MPa)	$0.5 + 2S_H$ (Sun et al., 2017)	Internal Friction Angle φ	25° (Sun et al., 2017)
E_{SH0} (MPa)	95[(Rutqvist et al., 2012; Yin et al., 2022b; Cheng et al., 2023)]	E_{SH1} (MPa)	670[(Rutqvist et al., 2012; Yin et al., 2022b; Cheng et al., 2023)]
Dilation angle ψ	0	Biot–Willis coefficient	1

2.3. Model validation

Given the lack of field-scale subsea CO_2 storage projects based on hydrates globally, direct validation of the model using actual engineering data is not feasible. Therefore, the model was validated against laboratory-scale experiments to evaluate its capability in reproducing the coupled thermal, hydraulic, and mechanical responses during CO_2 hydrate formation. To ensure the reliability of the numerical methodology, the model was validated against relevant laboratory-scale CO_2 hydrate storage experiments. Inui et al.(Yu et al., 2016) conducted laboratory tests on CO_2 hydrate formation and documented temporal variations in temperature, water production, and other key parameters. A model based on the experimental setup of Inui et al. is presented in Fig. 2. The computational domain is an axisymmetric cylinder with a radius of 25 mm and a height of 200 mm. For computational efficiency, a two-dimensional (2D) axisymmetric model was established, with mesh settings consistent with those detailed in Section 2.2 (Fig. 2). Similar to the reservoir model, the validation model adopted a free triangular mesh, comprising 4130 elements with an average element quality of 0.946. The model validation was performed by comparing simulation

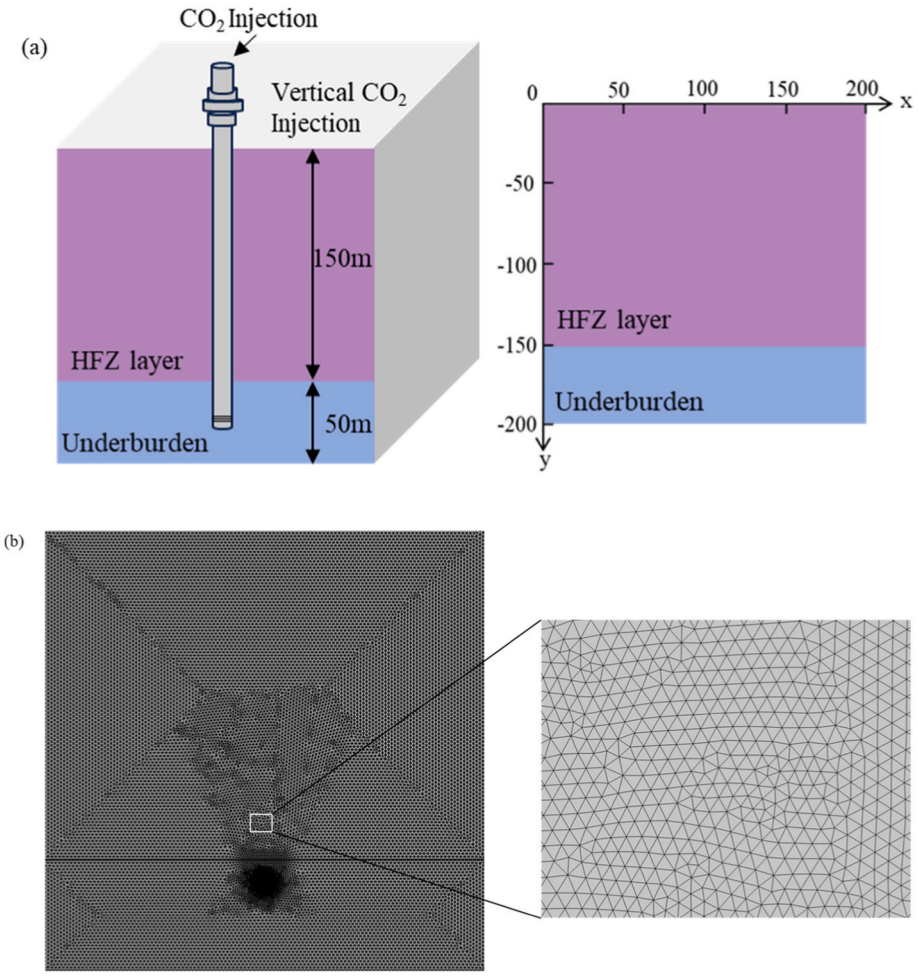


Fig. 1. (a) Model domain and (b) mesh distribution.

results with the experimental data from Inui et al. The initial injection temperature was set to 275.15 K, the injection pressure to 3.1 MPa, the CO_2 injection rate to 300 ml/min, and the injection duration to 19.1 min.

Fig. 3 presents the comparison between experimental and simulated temperatures during CO_2 injection. As shown in this figure, the simulated temperature profile exhibits a trend consistent with the experimental data, which indicates the model's capability to accurately capture the thermal evolution associated with CO_2 injection and hydrate formation. Although some discrepancies remain in the peak temperatures and their occurrence times, these differences can be attributed to porous-medium heterogeneity, stochastic hydrate formation, and heat exchange with the surroundings during the experiments. Compared with the simulation results reported by Yu et al. (Fig. 3b)(Yu et al., 2016), the present model reproduces the observed temperature evolution more realistically. While Yu's model exhibits relatively idealized step-like temperature increases, the temperature profiles predicted in this study are smoother and better capture the variations in peak temperatures and peak occurrence times among different monitoring locations, showing closer agreement with the experimental observations. Overall, the model accurately describes the heat generation, transfer, and dissipation processes during CO_2 hydrate formation.

Fig. 4 compared the simulated water production with experimental measurements, revealing general agreement between the two, with a calculated error of 10.18%. These comparisons confirmed the validity and reliability of the numerical model established in this study. Compared with the model developed by Yu et al. (Fig. 4a), which reported an error of 14.03%, the inclusion of the mechanical field in the present THMC-coupled model reduces the prediction error by 3.85%. This indicated that geomechanical effects improve the accuracy of fluid-flow prediction during CO_2 hydrate formation. The good agreement between simulation and experiment further validates the proposed THMC-coupled model.

To further validate the hydrate formation process and associated mechanical behavior, additional benchmarking has been conducted beyond the Inui experiment. Specifically, the model results are compared with the experimental and numerical data reported by Chen et al., including hydrate saturation evolution and stress–strain relationships. The comparison indicates that the model can reasonably reproduce both the hydrate formation characteristics and the corresponding geomechanical response. Together with the comparison of temperature evolution and water production, these results further support the model's capability in reproducing both hydrate formation and the associated geomechanical behavior. Detailed results of this supplementary validation are provided in the Supporting Information. This supplementary validation demonstrates the capability of the model to capture the fully coupled thermo-hydro-mechanical-chemical (THMC) processes. The laboratory-scale experiment was used to validate the model's ability to reproduce the key coupled processes under controlled conditions. Although scale-dependent effects may introduce uncertainty when extending the model to reservoir-scale simulations, the validation provides a reference for evaluating the coupled processes and storage performance at the reservoir scale.

Table 2
Model parameter settings.

Parameter	Value	Parameter	Value
porosity	0.32	capillary pressure model (Pa)	$P_c = P_0\left(\frac{S_L}{\frac{S_L+S_C}{(1-S_{Lr}-S_{Cr})}}-S_{Lr}\right)^{-nc}$
absolute permeability K_0 (mD)	2.38	P_0 (Pa)	10^6
sediment skeleton density (kg/m^3)	2800	nc	0.35
CO_2 hydrate density (kg/m^3)	1100	hydrate formation rate constant k_f ($mol/(m^2 \cdot Pa \cdot s)$)	0.35×10^{-3}
seawater density (kg/m^3)	1035	hydrate formation activation energy ΔE (J/mol)	81084
CO_2 density (kg/m^3)	determined by temperature and pressure	hydrate specific surface area A_{SH} (m^2)	$A_{SH} = \left(\frac{\phi^3}{2K}\right)^{1/2}$
permeability model (mD)	$K = K_0(1-S_H)^N$	CO_2 hydrate specific heat capacity $C_{p,H}$ ($kJ/kg/K$)	2.22
N	12	sediment skeleton specific heat capacity $C_{p,s}$ ($kJ/kg/K$)	1.00
relative permeability of the water phase (mD)	$k_{rL} = \left(\frac{S_L-S_{Lr}}{1-S_{Lr}}\right)^{n_L}$	sediment skeleton thermal conductivity λ_s ($W/(m\cdot K)$)	1.5
relative permeability of the CO_2 phase (mD)	$k_{rC} = \left(\frac{S_C-S_{Cr}}{1-S_{Cr}}\right)^{n_C}$	CO_2 hydrate thermal conductivity λ_H ($W/(m\cdot K)$)	0.49
S_{Lr}	0.2	reservoir Poisson's ratio	0.4
S_{Cr}	0.014	Young's modulus model	$E = E_{SH0} + (E_{SH1} - E_{SH0}) \times S_H$
n_L	4	n_C	2

3. Results and discussion

3.1. Single-well CO_2 injection: storage and reservoir deformation behavior

3.1.1. Long-term storage performance

Fig. 5 presents the CO_2 storage rate, cumulative storage amount, and mass distribution between free and hydrate phases after 5000 days of injection. Specifically, Fig. 5a shows the CO_2 storage rate and cumulative storage over the 5000 days injection period. The total stored CO_2 increased continuously with injection time, while the storage rate peaked and then declined rapidly, eventually stabilizing after approximately 5000 days. At the end of this period, the storage rate was 1135.20 kg/day and the total stored CO_2 reached 8.69×10^6 kg. Fig. 5c illustrates the evolution of CO_2 mass in the free and hydrate phases. Both phases showed progressive mass increases throughout the injection period. After 5000 days, the CO_2 mass in the free phase was 6.35×10^6 kg, while that in the hydrate phase was 2.34×10^6 kg, indicating that hydrate-phase CO_2 accounted for 27% of the total stored mass. Fig. 5d further demonstrates that as CO_2 injection continued and upward migration promoted hydrate formation, the proportion of the hydrate phase increased steadily. This trend corresponded to the three-stage model of CO_2 hydrate growth in silt sediments (Liu et al., 2025): (1) Rapid hydrate growth within the sand layer (first 1000 days), with saturation quickly reaching 19%; (2) Hydrate growth above the sand layer (by 3000 days), reaching 24% saturation; (3) Slower but sustained growth within the sand layer (3000–5000 days), with saturation increasing by only 3% to reach 27%.

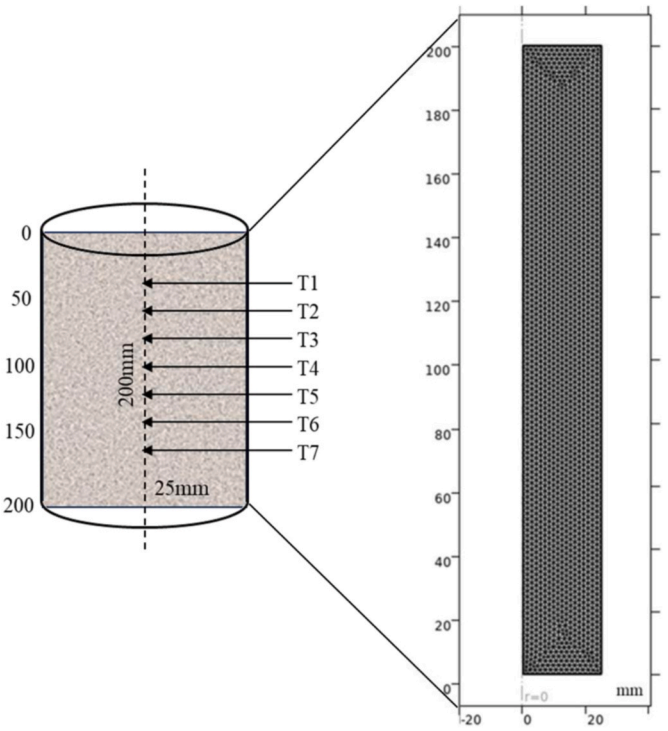


Fig. 2. Schematic of the validation model and mesh distribution.

As shown in Fig. 5b, CO_2 was continuously injected at a constant rate throughout the simulation period, resulting in a continuous increase in the cumulative injected CO_2 mass. The sequestration rate in Fig. 5a represents the combined sequestration rate of free-phase CO_2 and hydrate-phase CO_2. Although the sequestration rate gradually decreased after reaching its peak due to increased flow resistance, it remained positive throughout the simulation period, leading to a continuous increase in the cumulative sequestration mass. The cumulative injected CO_2 mass exceeded the cumulative sequestration mass because part of the injected CO_2 remained in an active migration state and was not retained within the defined sequestration domain. Therefore, only free-phase CO_2 and hydrate-phase CO_2 retained within the sequestration domain were included in the reported sequestration mass.

Fig. 6 presents the spatial distribution of hydrate saturation, CO_2 saturation, temperature, and pressure during CO_2 storage. After CO_2 was injected into the subsea reservoir, it diffused outward from the wellbore. By approximately 1000 days, it had reached the hydrate formation zone and began to form hydrates. As more CO_2 diffused upward, the lateral extent of the hydrate cap expanded. After 5000 days, the cap reached a lateral width of approximately 50 m (Fig. 6a). The upward migration of CO_2 and subsequent hydrate formation lowered the CO_2 saturation in the formation zone. The developing hydrate layer impeded further vertical migration, diverting CO_2 to spread laterally beneath the cap (Sun et al., 2024). The resulting hydrate saturation remained relatively low, with most CO_2 retained in the free phase. After 5000 days, CO_2 had diffused laterally within the reservoir to a width of about 60 m (Fig. 6b). The observed upward migration of CO_2 and the lateral expansion beneath the hydrate cap are strongly influenced by wettability. Under water-wet conditions, CO_2 acts as the non-wetting phase and preferentially occupies pore centers, which enhances capillary resistance to vertical flow and promotes lateral spreading, consistent with Fig. 6a and b. Meanwhile, hydrate formation at CO_2–water interfaces may alter pore surface properties and constrict flow channels, modifying capillary forces and reinforcing CO_2 redistribution, leading to the dominance of free-phase CO_2 and relatively low hydrate saturation(Khoramian et al., 2025b, 2026b). Following the onset of injection, pressure near the

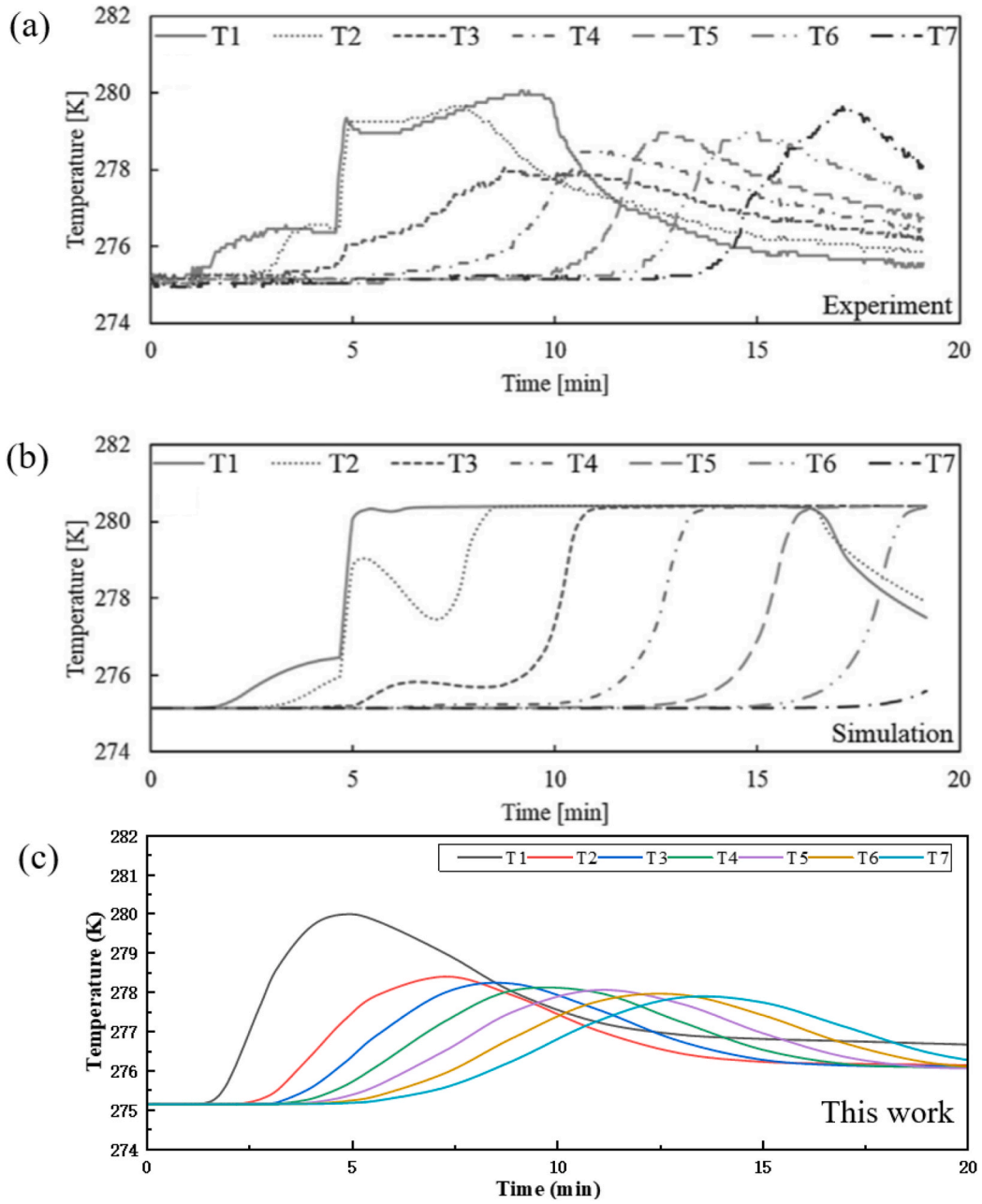


Fig. 3. Comparison of temperature during CO_2 injection at 275.15 K: (a) experimental results; (b) Yu's simulated results and (c) the simulation results of this work.

wellhead rose continuously, forming a localized high-pressure zone within the CO_2 diffusion region. Pressure propagation was influenced by factors such as well location, reservoir permeability, and fluid flow. After injection ceased, the pressure gradient stabilized, with the final pressure distribution closely matching the CO_2 diffusion zone (Fig. 6c). Given that CO_2 was injected at a relatively high temperature and the formation of hydrates released heat, coupled with the low thermal conductivity of the reservoir, the heat did not dissipate promptly. This resulted in the emergence of a localized high - temperature zone near the wellhead, as presented in Fig. 6d.

Fig. 6e and f illustrate the variations in reservoir strain and displacement during the CO_2 sequestration process. The formation of CO_2 hydrates leads to significant pore blockage, which not only enhances mechanical stability but also indirectly regulates the dissolution trapping process by altering the pore specific surface area and fluid connectivity. As noted in the reactive transport simulations of (Khoramian et al., 2026c), the coupled effects of temperature, salinity, and wettability ultimately dictate the overall storage efficiency. Following CO_2 injection, pore pressure increased rapidly, leading to stress redistribution within the reservoir until a new mechanical equilibrium was established. Volumetric strain exhibited a close correlation with pore pressure changes; wherein higher pore pressure resulted in greater volumetric deformation. Significant volumetric strain was concentrated primarily in the hydrate cap layer, reaching a maximum value of approximately 0.005. The increase in mechanical strength and the reduction in effective stress, both induced by CO_2 injection and subsequent hydrate formation, contributed to sediment deformation and associated vertical displacement of the formation. As pressure rose, noticeable displacement developed within the reservoir, with a maximum vertical displacement of approximately 0.2 m. The injection of CO_2 into reservoir pores and the ensuing formation of hydrates elevated pore pressure, resulting in expansion of the pore space. Over time, this expansion induced uplift of the overlying strata, which likely constitutes the primary mechanism for the observed increase in vertical

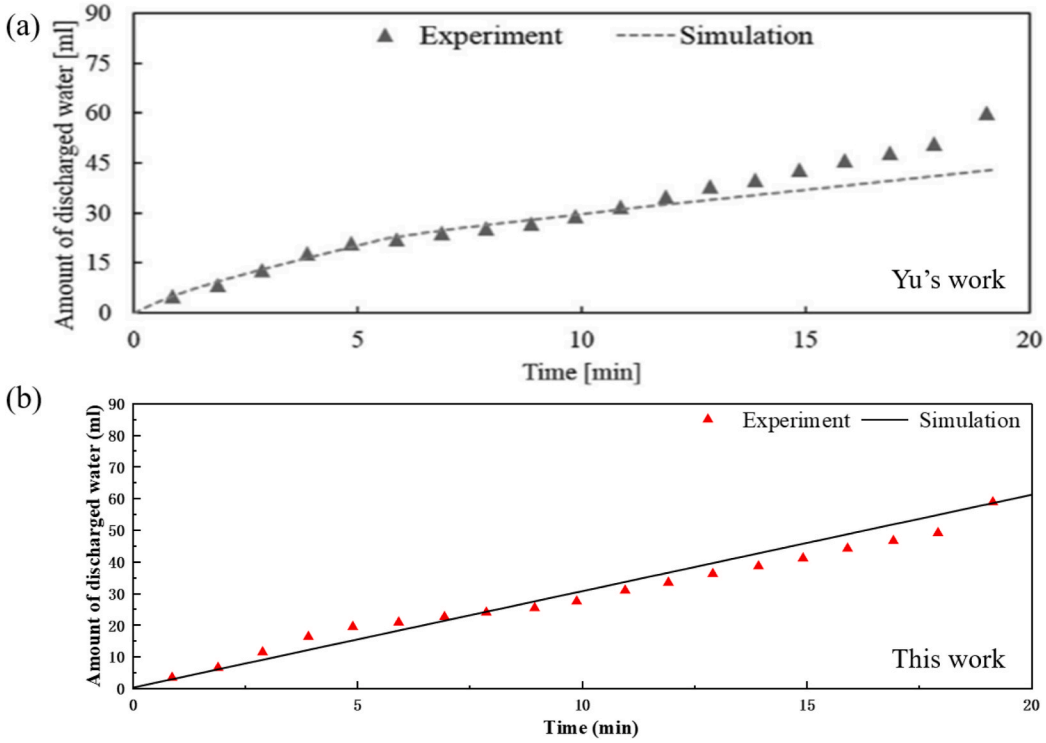


Fig. 4. Experimental and simulated results of water production during CO_2 injection at 275.15 K: (a) Yu's work and (b) this work.

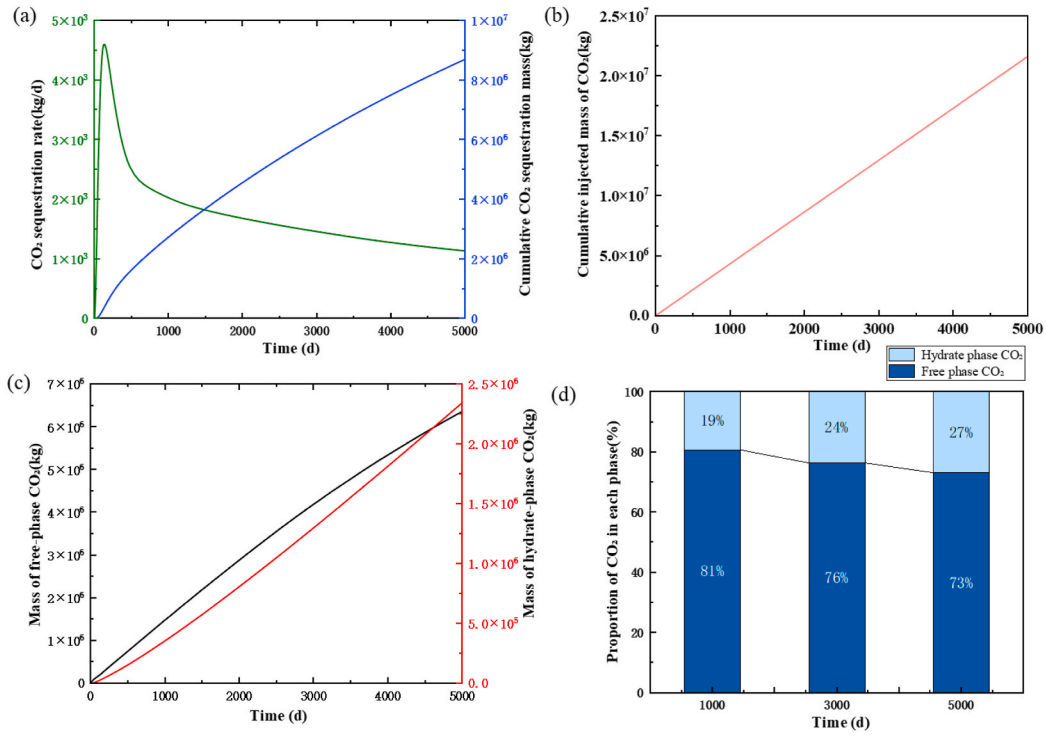


Fig. 5. Evolution of CO_2 sequestration performance: (a) cumulative sequestration mass and sequestration rate; (b) cumulative injected CO_2 mass; (c) cumulative hydrate mass; and (d) phase distribution of CO_2.

formation displacement. Fig. 6 illustrates the spatial distribution and evolution of CO_2 hydrate formation and reservoir deformation. To further quantify the stress and deformation characteristics of the reservoir, the variations in vertical stress, horizontal stress, and vertical and horizontal displacements with depth and distance from the injection well are analyzed in the following sections.

3.1.2. *Reservoir deformation*

The shear strength and pore pressure of sediments played a critical role in maintaining reservoir stability (Ning et al., 2012)。Throughout

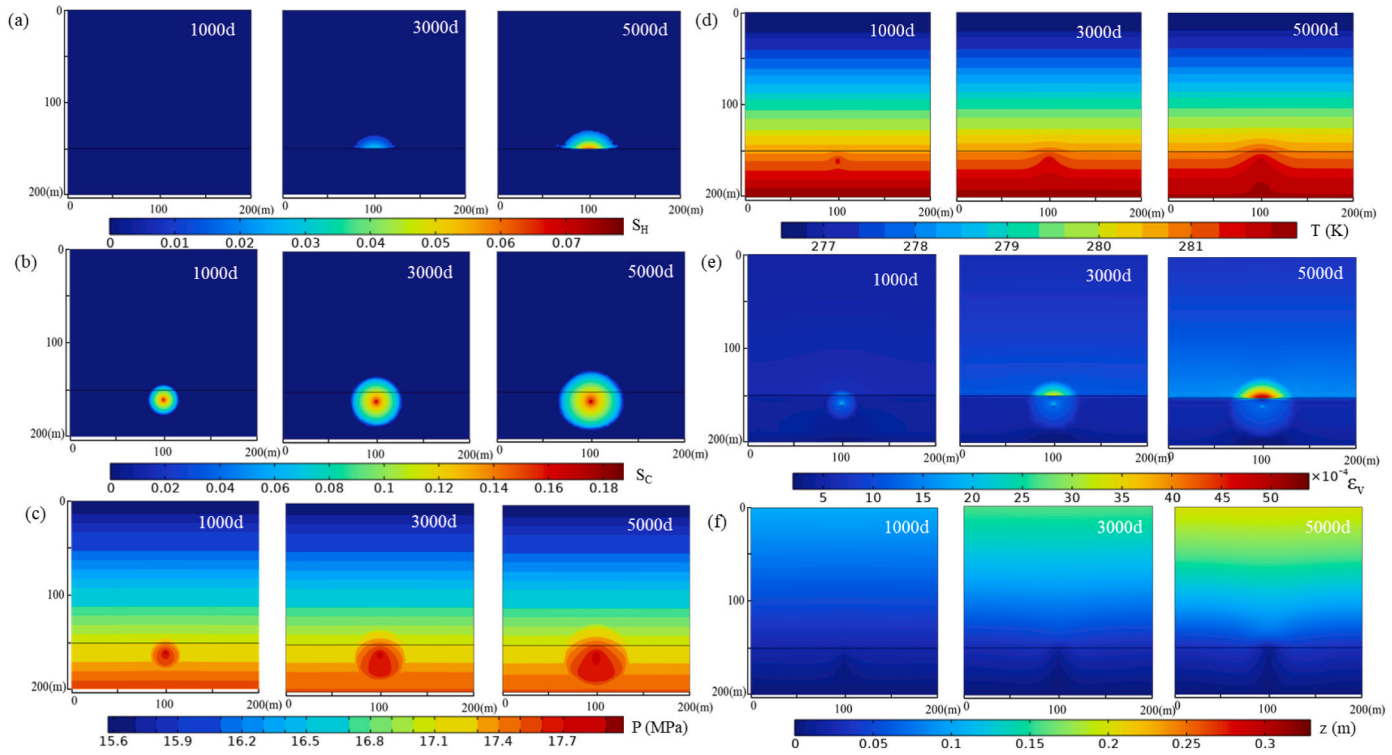


Fig. 6. Spatial distributions of the simulated physical fields at 1000, 3000, and 5000 days of vertical CO_2 injection: (a) hydrate saturation, (b) CO_2 saturation, (c) pressure, (d) temperature, (e) volumetric strain, and (f) displacement.

the CO_2 sequestration process, the deviatoric stress demonstrated a gradual increase in tandem with axial strain. Throughout the CO_2 sequestration process, the deviatoric stress increased gradually, while the hydrate-bearing cap layer exhibited localized deformation and stress redistribution due to CO_2 injection and hydrate formation. Fig. 7 illustrates the variation in effective stress within the reservoir during CO_2 hydrate sequestration, with the injection point located at (100, −160). The vertical coordinate is referenced to the reservoir top (y = 0 m), and negative values denote locations below the reference level. Therefore, increasing depth corresponds to decreasing y-coordinate values. As shown in Fig. 7a, the vertical effective stress increased linearly with depth but exhibited significant disturbance near the injection point. This phenomenon was mainly attributed to the rapid changes in pore pressure, hydrate saturation, and effective stress near the injection well during CO_2 injection and hydrate formation, which induce localized deformation and stress redistribution within the reservoir. At this stage, detached hydrate particles tended to form cemented aggregates with surrounding sand, while isolated hydrate particles helped maintain nearby sand grains near their original positions. This behavior suggests a localized reinforcement effect of hydrates on the sediment skeleton, which temporarily enhanced structural stability despite ongoing deformation (Wu et al., 2020a). The change in effective stress was closely linked to pore pressure—an increase in pore pressure resulted in a reduction of effective stress. After 5000 days of injection, a pronounced decrease in effective stress was observed near the injection point, indicating that the pore pressure rise induced by CO_2 injection attenuated the initial in-situ stress. As shown in Fig. 7b, the distribution of horizontal principal effective stress exhibited spatial heterogeneity in its evolution. Near the interface region (y = −50 m), the upward migration of CO_2 and subsequent hydrate formation reduced local pore pressure,

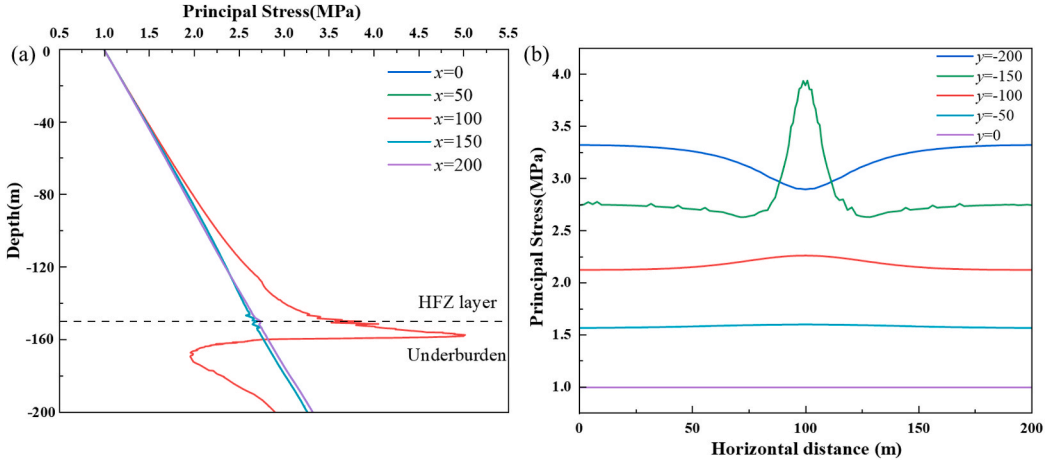


Fig. 7. Variations of (a) vertical effective stress and (b) horizontal effective stress along different planes of the reservoir.

thereby increasing the effective principal stress in that area. This stress redistribution suggested that hydrate formation can locally strengthen the sediment skeleton, whereas adjacent zones may still undergo stress relaxation due to fluid overpressure. Overall, CO_2 injection and hydrate formation led to increased pore pressure and volumetric expansion within the reservoir, which reduced effective stress and altered the in-situ stress field. As deformation progressed, localized tensile or shear stresses could exceed the strength threshold of hydrate-bearing sediments, potentially causing micro-failure or damage to the hydrate cementation structure (Wu et al., 2020b). Such mechanical weakening and related instability underscore the importance of a comprehensive assessment of long-term storage safety, particularly in terms of the mechanical integrity of hydrate-bearing layers under prolonged CO_2 injection and storage conditions.

Fig. 8 presents the temporal evolution of stress at four monitoring points situated 20 m from the wellhead in different directions. Initially, due to the continuous CO_2 injection, stress at all four points exhibited a similar declining trend. Approximately 3000 days into the process, stress at the monitoring point (100, −140), located within the hydrate formation zone, commenced a gradual increase. This is likely attributable to the reduction in capillary pressure accompanying hydrate formation. Moreover, at the same hydrate saturation level, the disparity in capillary pressure across different directions widened. Meanwhile, stress at the three monitoring points in the underlying formation persisted in decreasing, leading to an overall increase in the formation's heterogeneity (Wang et al., 2021).

Fig. 9 presents the displacement response of the reservoir during CO_2 injection, illustrating both the vertical (Fig. 9a) and horizontal (Fig. 9b) displacement distributions along the injection profile. The results indicate that CO_2 injection, driven by seepage forces and elevated pore pressure, induced a rapid increase in displacement and notable reservoir uplift. In contrast to previous studies that primarily focused on the influence of geostress on reservoir permeability (Wang et al., 2023b), the present analysis highlights the role of fluid-induced pressure changes in driving deformation. Due to the fixed boundary condition at the base of the computational domain, displacement was most pronounced at the seafloor. By the end of injection, the maximum seabed uplift reached approximately 0.2 m. Although no geological failure was predicted under the simulated conditions, such deformation may have potential implications for subsea infrastructure and should be considered in engineering assessments. The region near the injection well exhibited less uplift compared to surrounding areas. This may be attributed to the localized high-pressure zone generated by fluid dynamics during injection, which did not directly translate into uplift but instead transmitted pressure and induced deformation further from the wellbore. The simulated seabed uplift provides an indication of the potential geomechanical response associated with CO_2 injection and hydrate formation. Although the present model does not explicitly simulate subsea infrastructure, localized seabed deformation may affect the stability and serviceability of seafloor facilities. Therefore, the predicted deformation should be considered in conjunction with site-specific infrastructure layouts and allowable deformation limits in future engineering applications.

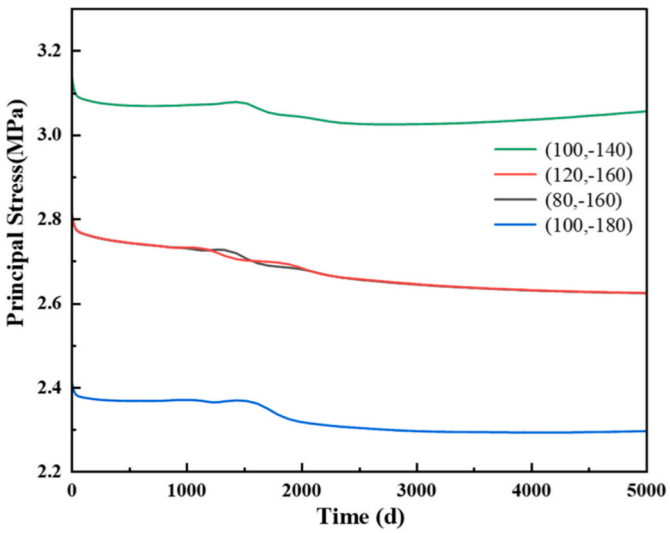


Fig. 8. Stress variation at each monitoring point over time.

Fig. 10a illustrates the relationship between maximum reservoir displacement, average reservoir stress, and total CO_2 storage during the sequestration process. The results indicated that increasing CO_2 storage triggered a notable mechanical response in the reservoir. As storage accumulated, reservoir displacement increased nonlinearly, rising more rapidly in the early stage and gradually slowing thereafter. This pattern suggests that most of the pore-volume change occurred during the initial phase of storage. Concurrently, average reservoir stress decreased continuously with increasing storage, with a steeper decline in the early stage that later stabilized. This trend reflects rapid stress release at the beginning of storage, followed by a gradual approach toward mechanical equilibrium. Fig. 10b further shows that the vertical displacement at both the seafloor and the base of the hydrate formation zone increases with injection time. The seafloor displacement remains larger than that at the base of the hydrate formation zone and reaches approximately 0.20 m at 5000 days. Overall, these variations demonstrate that CO_2 injection reduced effective stress in the reservoir and induced expansion-related deformation. Consequently, both deformation and stress evolution must be fully accounted for in storage design and monitoring to ensure long-term storage safety.

3.1.3. *Reservoir stability analysis*

Fig. 11 presents the evolution of the effective principal stress at four selected points along a reservoir profile, together with the critical failure line defined by the Mohr-Coulomb criterion. Fig. 11a, b, and 11c correspond to stress variations during CO_2 injection at rates of 0.05 kg/s, 0.1 kg/s, and 0.5 kg/s, respectively, over a period of 5000 days. The rise in pore pressure reduced both the vertical and horizontal effective stresses near the well, but did not generate significant deviatoric stress. The mechanical stability was evaluated using the Mohr–Coulomb elastoplastic model, and the simulated stress state did not reach the yield condition, indicating that no shear failure occurred under the simulated conditions. As shown in Fig. 11a, at an injection rate of 0.05 kg/s, the stress change in the reservoir after 5000 days remained minor. The principal effective stress paths curved away from the yield line, indicating that no formation failure occurred. Similarly, increasing the injection rate to 0.1 kg/s and 0.5 kg/s showed that variations in flow rate had limited influence on reservoir stress and, within the studied range, did not induce yielding (Fig. 11b and c). To examine stress behavior under higher injection intensities, Fig. 11d, e, and 11f show the stress responses for CO_2 injection at rates of 1 kg/s, 2 kg/s, and 4 kg/s over durations of 4000 days, 2000 days, and 1000 days, respectively. The different durations were selected to ensure the same cumulative injected CO_2 mass among the three cases, allowing the effect of injection rate on stress behavior to be examined. The results demonstrate that higher injection rates expanded the CO_2 diffusion range and further elevated pore pressure, resulting in more pronounced stress changes in the formation. Nevertheless, shortening the storage duration for a given injection rate can effectively mitigate the risk of formation fracturing. It should be noted that the present model does not explicitly account for time-dependent creep behavior. Therefore, the predicted deformation and stress responses are subject to uncertainty over longer time scales, and the influence of creep on the long-term stability of CO_2 hydrate storage should be investigated in future studies.

Well injection capacity was a key factor in studying fluid–rock interactions and had a significant impact on multiphase distribution and flow processes. These factors were also related to the selection of CO_2

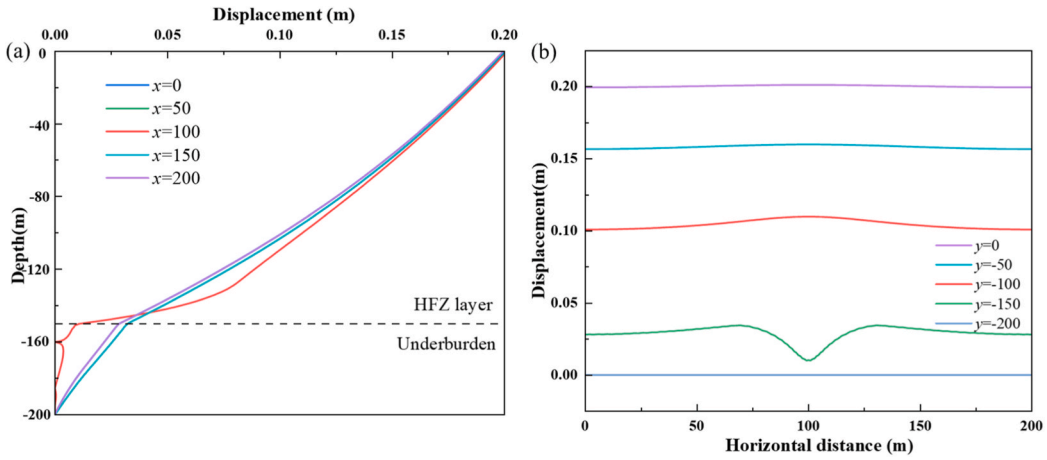


Fig. 9. Variation of reservoir displacement with distance on different planes: (a) vertical displacement and (b) horizontal displacement.

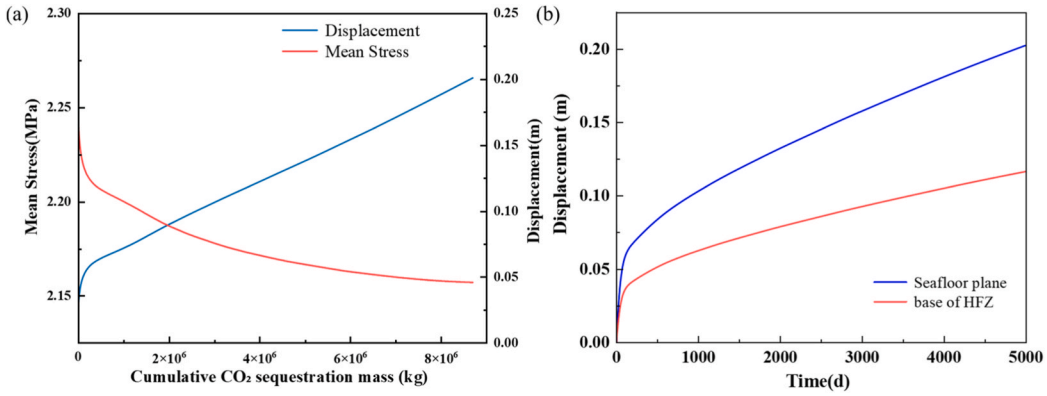


Fig. 10. Reservoir deformation during CO_2 sequestration: (a) displacement and average stress with total CO_2 storage in a single-well system; (b) vertical displacement over time.

storage sites (Cui et al., 2018). Fig. 12 showed the spatial distribution comparison of hydrate saturation, CO_2 saturation, and CO_2 flux at the end of the simulation under different injection rates. As the injection rate increased, the area of the hydrate cap layer expanded significantly. When the injection rate was 0.1 kg/s, the width of the hydrate cap layer increased by about 30 m compared to the case with 0.05 kg/s. The CO_2 saturation near the wellhead increased, and both the distribution range and saturation of CO_2 were significantly higher. When injected at 0.1 kg/s, the CO_2 saturation near the wellhead increased by about 0.12 compared to 0.05 kg/s, indicating that CO_2 not converted into hydrates accumulated in the reservoir. The injection rate distribution showed that a higher injection rate increased the flow velocity and diffusion range, promoting transport, but it also increased pressure disturbances, which can affect formation stability.

To quantitatively evaluate the influence of injection rate on storage performance, the mass and fraction of CO_2 in both the free and hydrate phases, as well as the storage rate and total storage, were calculated for different injection rates. As shown in Fig. 13, increasing the injection rate significantly affected the total CO_2 storage and the mass distribution between phases. A higher injection rate substantially raised the peak storage rate in the reservoir, though the rate still declined rapidly thereafter. Although the peak sequestration rate temporarily exceeds the injection rate, this peak represents a transient response associated with the rapid stabilization of previously injected CO_2 within the reservoir. The cumulative sequestration mass remains lower than the cumulative injected mass throughout the simulation period, ensuring mass conservation. Moreover, increasing the injection rate reduced the mass of CO_2 converted into hydrates, thereby lowering the hydrate phase fraction. When the injection rate increased from 0.01 kg/s to 0.1 kg/s, the total CO_2 storage grew by 22.7 times, while the hydrate phase fraction decreased from 29% to 26%. This trend likely resulted from the fact that a lower injection rate favored CO_2 diffusion, enabling more complete reaction with pore water and thus enhancing the hydrate conversion rate.

3.1.4. *Effect of reservoir deformation on CO_2 storage performance*

To evaluate the impact of neglecting mechanical behavior on the prediction of CO_2 storage dynamics, a THC-coupled model that omitted mechanical changes during gas injection was also used to simulate the sequestration process. A comparison between the simulation results of the THC and THMC models is presented in Fig. 14. Reservoir deformation can inhibit pressure propagation and heat transfer within the formation, thereby hindering CO_2 injection and hydrate formation. When mechanical deformation was disregarded, the simulated masses of hydrates and stored CO_2 after 5000 days of sequestration were 8.26×10^6 kg and 8.82×10^6 kg, respectively. Compared with the THC model, the THMC model, which accounted for deformation, predicted 2.04% lower hydrate mass and 1.42% lower CO_2 storage. This demonstrates that omitting reservoir deformation in CO_2 hydrate storage simulations leads to an overestimation of long-term CO_2 storage and hydrate formation potential. This reduction was mainly attributed to the feedback between sediment deformation and fluid flow, whereby deformation altered the pore structure and resulted in a more pronounced reduction in permeability, thereby restricting CO_2 migration and subsequent hydrate formation. These results indicate that neglecting reservoir deformation may lead to an overestimation of long-term

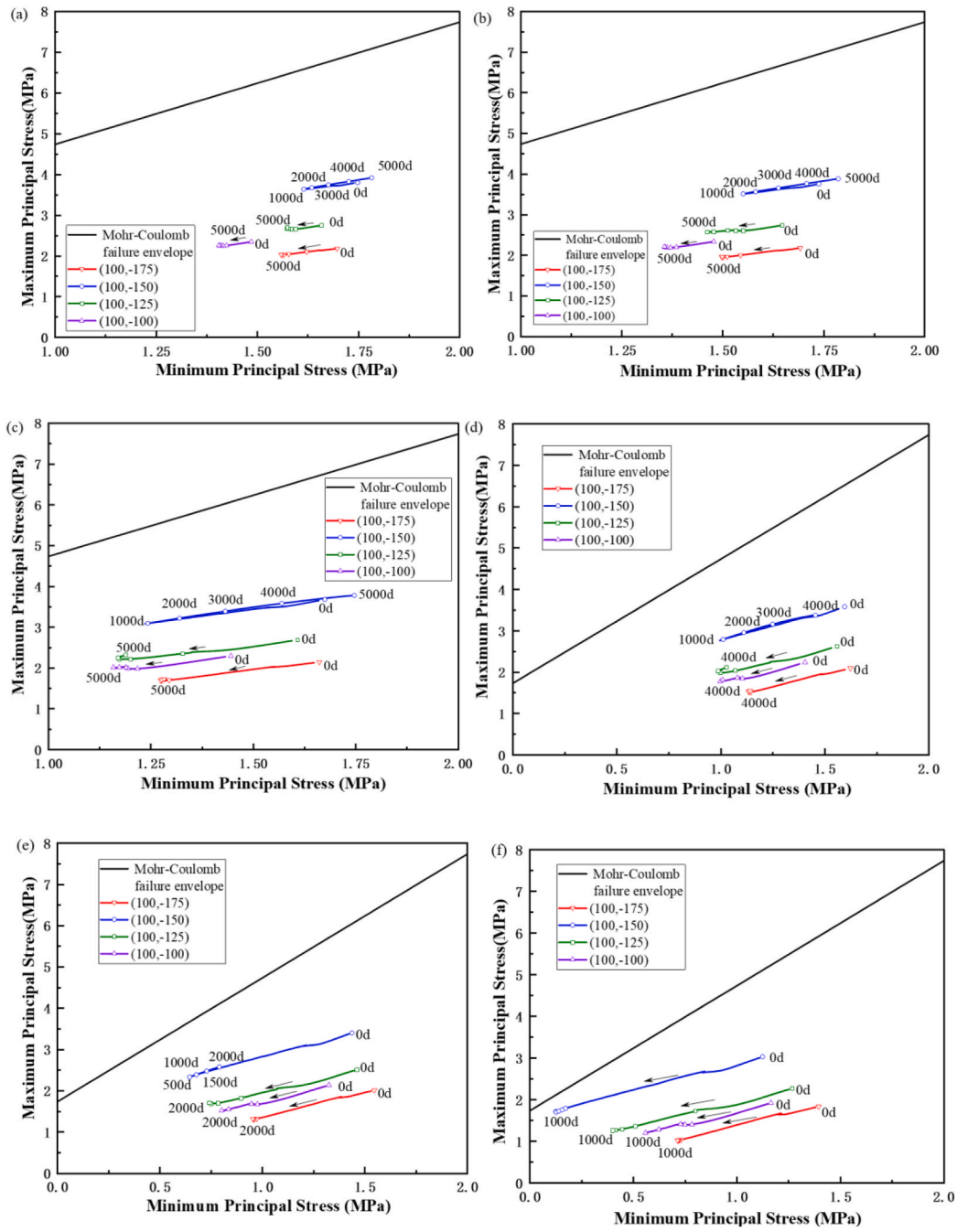


Fig. 11. Comparison of the effective principal stress curves at different reservoir points with the Mohr-Coulomb failure criterion for sediment failure: (a) injection rate 0.05 kg/s, (b) injection rate 0.1 kg/s, (c) injection rate 0.5 kg/s, (d) injection rate 1 kg/s, (e) injection rate 2 kg/s, (f) injection rate 4 kg/s.

CO_2 storage and hydrate formation potential. These results underscore that reservoir deformation plays a non-negligible role in governing CO_2 storage and hydrate formation behavior. Although the difference in total storage is only ~1.42%, the practical significance of THMC coupling lies beyond bulk volume estimation. This indicates that mechanical coupling has a limited effect on the overall storage capacity under the present conditions but remains important for evaluating sediment deformation and reservoir property evolution. It significantly improves the characterization of sediment deformation and reservoir-property evolution, which are important for assessing the long-term safety of subsea CO_2 hydrate storage. The added model complexity is justified by its ability to capture coupled geomechanical effects that are absent in THC simulations, including stress redistribution and permeability evolution. These are critical for evaluating reservoir safety, caprock stability, leakage risk, and long-term system performance.

To further examine the influence of mechanical deformation on reservoir sediments, changes in average porosity and permeability over 5000 days were calculated using the THC model, as presented in Fig. 15. When mechanical deformation was neglected, reservoir sediments experienced no compaction; consequently, at the end of the storage period, average porosity was 0.0007 higher and permeability 0.10 mD greater compared to the THMC model, which incorporated mechanical effects. The THMC model exhibited a permeability reduction of 13.53%, which exceeded that of the THC model (9.37%). Thus, omitting mechanical deformation led to smaller reductions in reservoir porosity and permeability, creating more favorable conditions for pressure propagation and heat transfer. This enhanced fluid flow through the pore network and ultimately resulted in an overestimation of CO_2 storage

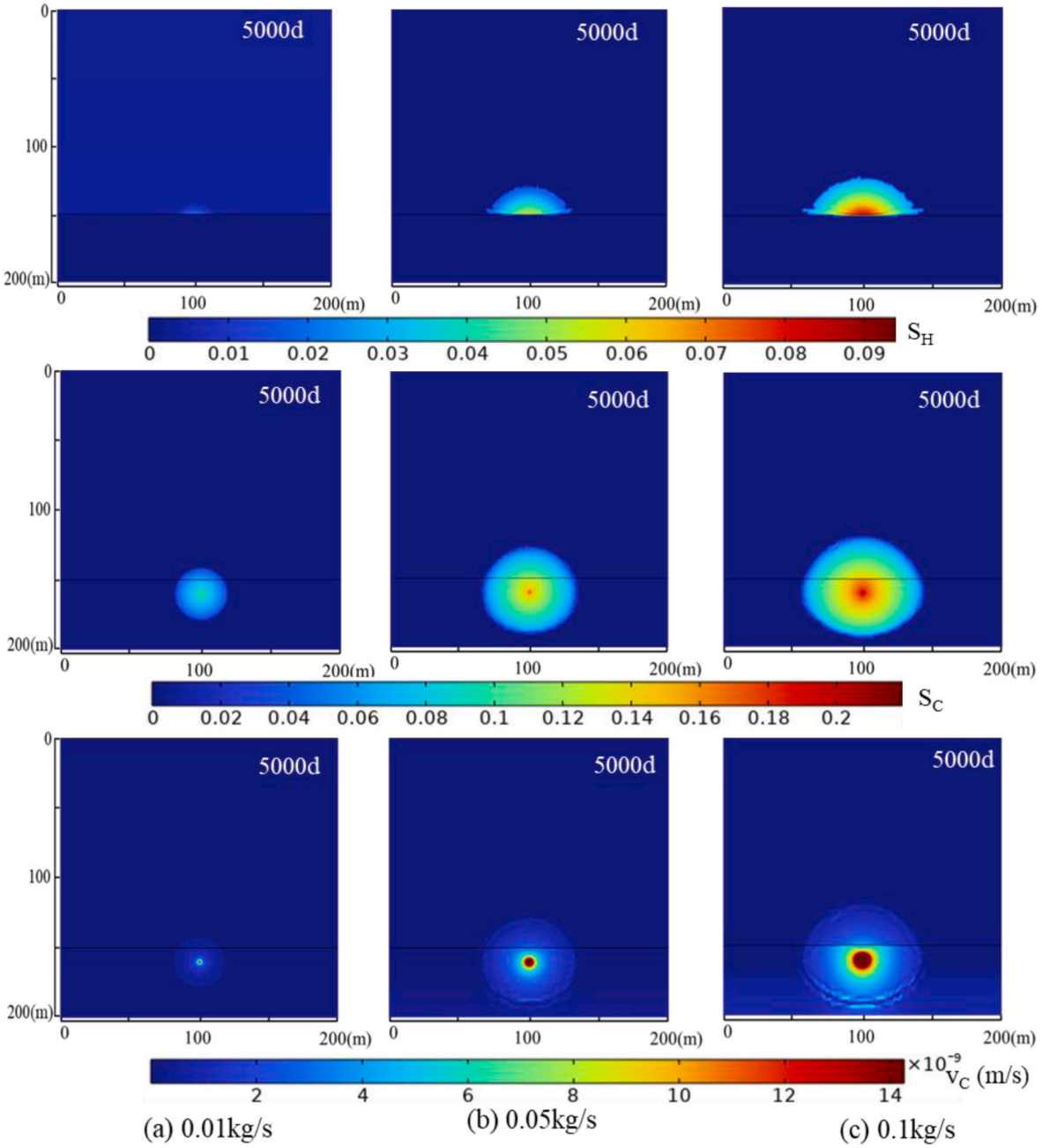


Fig. 12. Distribution of reservoir hydrate saturation, CO_2 saturation, and CO_2 flow rate under different injection rates.

capacity.

3.1.5. Sensitivity analysis

To improve the robustness of the simulation results, a sensitivity analysis of key parameters is conducted. Among them, permeability and temperature are critical factors controlling CO_2 migration, hydrate formation, and storage performance. Permeability governs fluid flow and pressure distribution, while temperature determines hydrate stability and phase behavior. Therefore, this study focuses on evaluating the effects of these two parameters on CO_2 transport and hydrate-based sequestration.

Fig. 16 illustrated the spatial distribution characteristics of CO_2 saturation (S_C), hydrate saturation (S_H), and permeability (K) evolution in the reservoir 5000 days after injection, under different initial permeability conditions (2.38mD, 5mD, 10mD). Simulation results indicated that as the initial permeability increased from 2.38mD to 10mD, CO_2 exhibited enhanced diffusivity driven by buoyancy and injection pressure differentials, with its saturation field (S_C) showing pronounced lateral expansion. Under high-permeability conditions (10mD), CO_2 rapidly penetrated the deep rock matrix and dispersed laterally. In contrast, under low-permeability conditions (2.38mD), CO_2 migration was significantly constrained by pore structures, resulting in substantial accumulation of liquid CO_2 above the injection point and at the bottom interface of the hydrate formation zone (HFZ). In the low-permeability group (2.38mD), the concentrated CO_2 accumulation at the interface promoted intense contact and reaction between water and CO_2, inducing the formation of high-saturation hydrates (peak S_H approached 0.06). The permeability distribution revealed that hydrate precipitation occupied the original pore space, leading to a sharp reduction in effective permeability at the interface, thereby forming a hydrate cap that impeded further CO_2 migration. Although high-permeability (10mD) reservoirs exhibited lower flow resistance at the

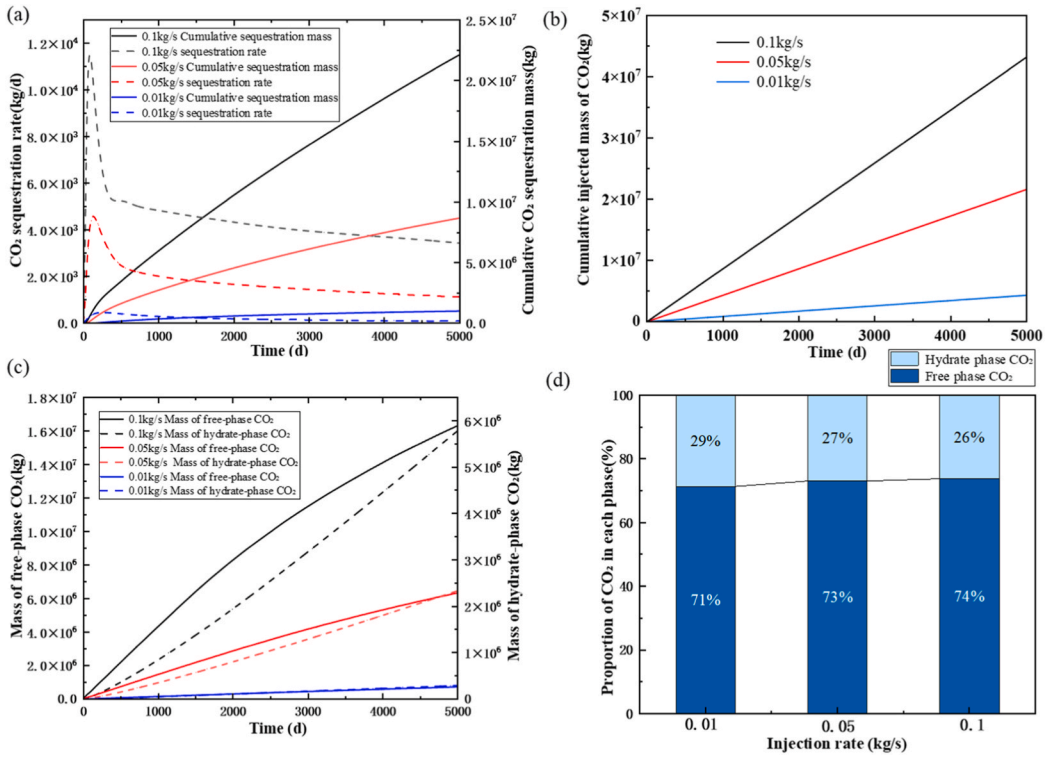


Fig. 13. Effect of injection rate on CO_2 storage performance: (a) changes in total CO_2 storage and storage rate; (b) cumulative injected CO_2 mass; (c) CO_2 mass in the free phase and hydrate phase; (d) fraction of CO_2 in each phase.

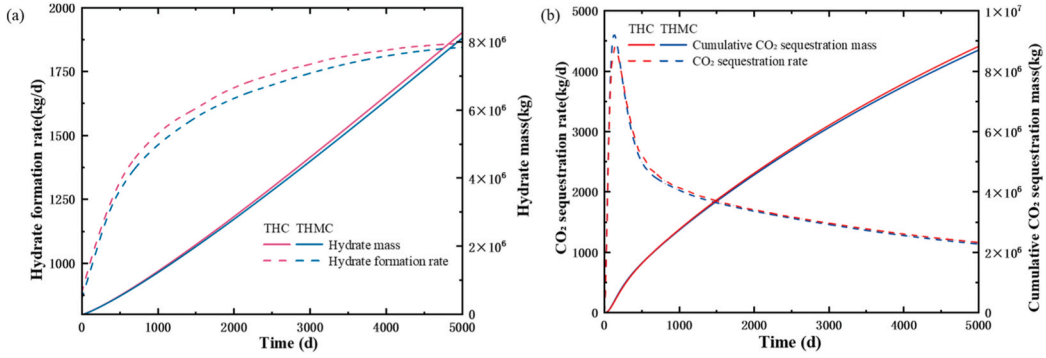


Fig. 14. Comparison between THMC and THC models: (a) hydrate formation mass and rate, and (b) CO_2 storage mass and rate.

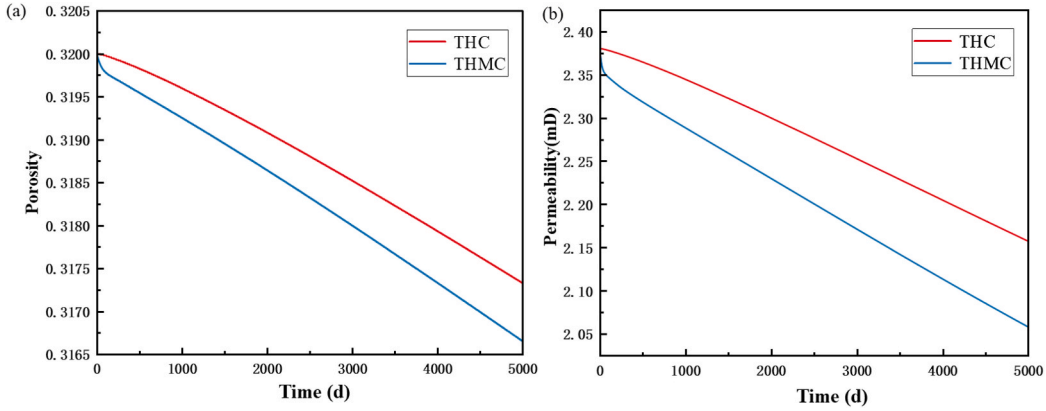


Fig. 15. Comparison of the THMC and THC models: (a) porosity and (b) permeability.

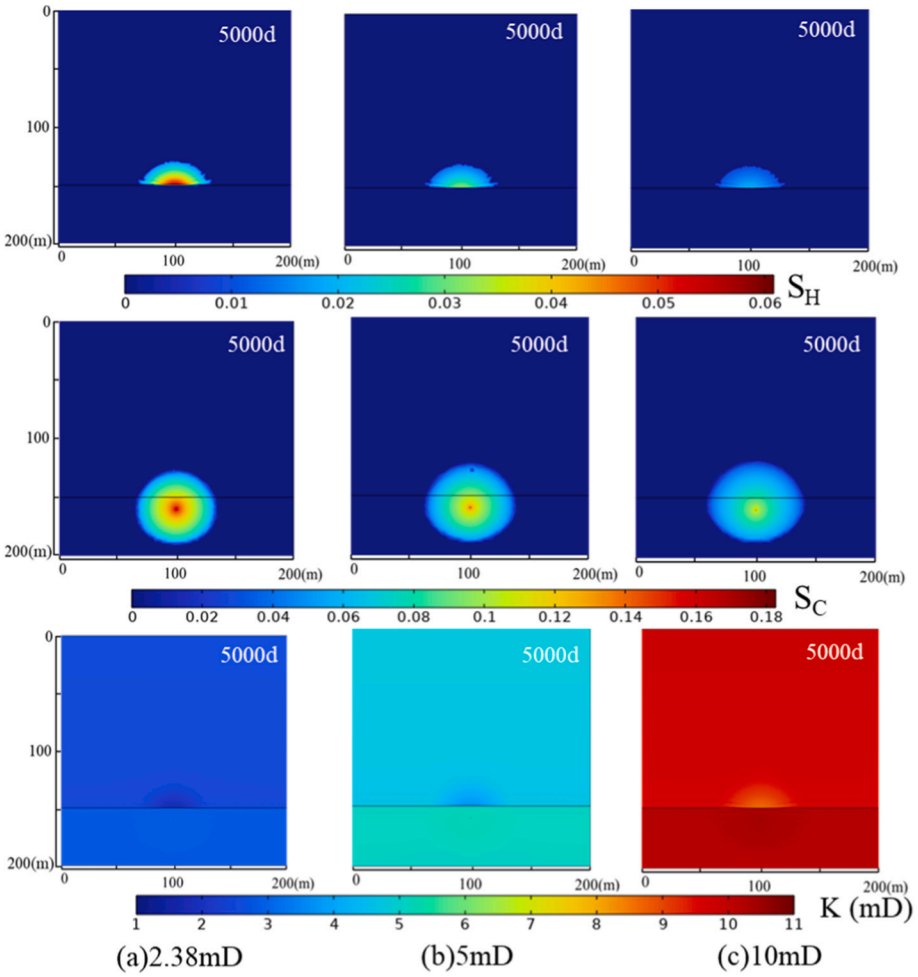


Fig. 16. Distribution of reservoir hydrate saturation, CO_2 saturation, and CO_2 flow rate under different initial permeabilities.

initial injection stage, the resulting hydrate layers were more dispersed and exhibited lower saturation, making it difficult to form an effective continuous seal. In contrast, low-permeability reservoirs, while limiting the diffusion rate of CO_2, induced the formation of a dense hydrate cap that more effectively blocked the risk of CO_2 leakage into the deep-sea environment.

Fig. 17 presented the variations in CO_2 storage rate, total storage capacity, and two-phase ratio under different initial permeability conditions. In terms of storage scale, high permeability (10mD) significantly improved injection efficiency, with the cumulative storage capacity over 5000 days being approximately 1.8 times that of the 2.38mD group. Regarding storage stability, low-permeability reservoirs offered greater advantages, with the hydrate-phase CO_2 accounting for as much as 27%, representing an 11% increase compared to the 10mD group. These results indicated that low permeability restricted the frontal migration of CO_2, inducing localized enrichment at the reaction interface and the formation of high-saturation hydrates, thereby generating a hydrate cap that significantly reduced effective permeability at the interface.

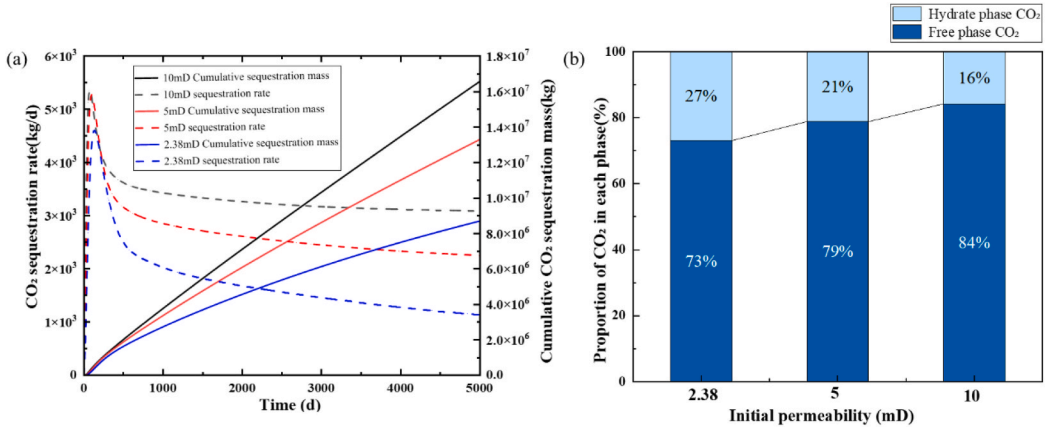


Fig. 17. (a) CO_2 sequestration rate and total CO_2 sequestered, and (b) two-phase fraction under various initial permeabilities.

Consequently, while high permeability facilitated rapid CO_2 injection, medium-to low-permeability reservoirs enhanced CO_2 hydrate conversion and cap formation, demonstrating superior long-term storage security and leakage prevention potential.

Fig. 18 illustrated the distributions of hydrate saturation, CO_2 saturation, and temperature field in seafloor sediments under different injection temperature conditions at 5000 days. The contour results indicated that, at 5000 days, the overall distribution characteristics of hydrate saturation, CO_2 saturation, and temperature field were generally consistent across different injection temperature conditions. Hydrates were predominantly generated in the hydrate formation zone surrounding and above the wellbore, with the peak saturation and distribution range showing no significant variation with injection temperature. Free-phase CO_2 also formed similar enrichment zones around the wellbore, with minor differences among the cases. Localized temperature variations were observed only near the wellbore, where higher injection temperatures led to a slight increase in local temperature; however, the thermal influence was limited and did not significantly alter the overall thermal structure or hydrate stability conditions of the reservoir. Collectively, within the injection temperature range of 280.15 K to 284.15 K, the injection temperature exhibited a minor effect on CO_2 hydrate storage performance. This was likely because, under the low injection rate conditions, CO_2 rapidly reached thermal equilibrium with the surrounding reservoir upon injection, without substantially altering the overall thermal structure of the reservoir.

Quantitative analysis indicated that the injection temperature within the range of 280.15 K to 284.15 K exerted a minor influence on the overall CO_2 storage performance (Fig. 19). The storage rate and cumulative storage capacity curves under different temperature conditions exhibited a high degree of overlap, with the total storage capacity at 5000 days remaining around 8.8×10^6 kg across all cases. Variations in injection temperature did not alter the final phase partitioning ratio of CO_2 within the reservoir, and the hydrate-phase fraction remained consistently stable at 27%. These results suggest that the deep-sea low-

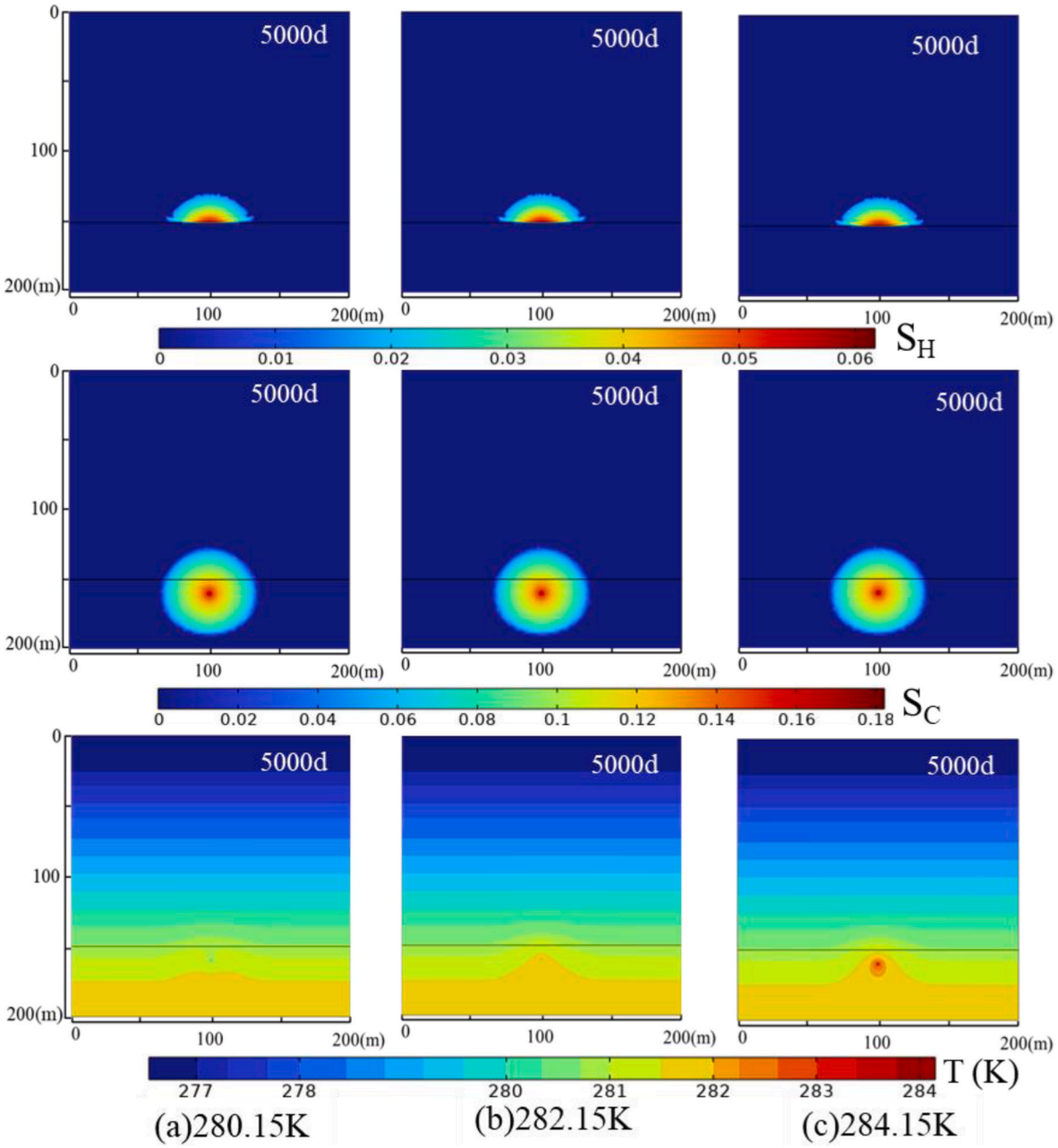


Fig. 18. Distribution of reservoir hydrate saturation, CO_2 saturation, and CO_2 flow rate under different injection rates.

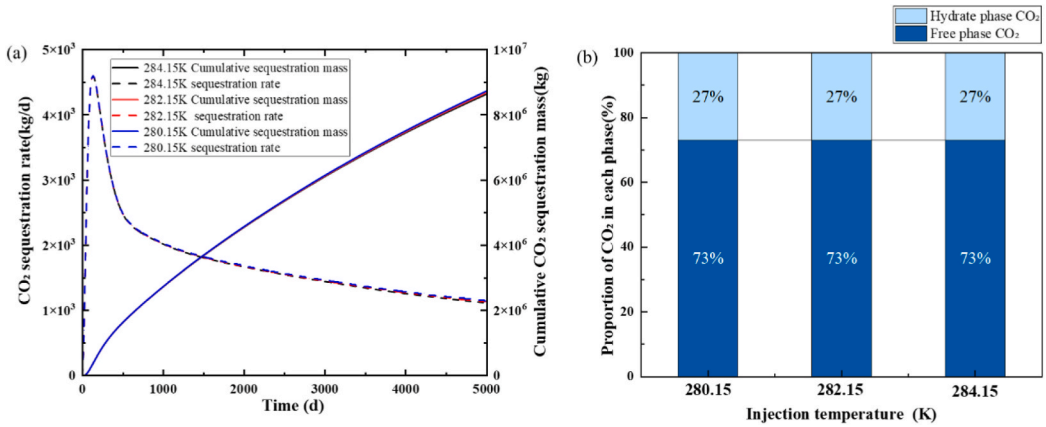


Fig. 19. (a) CO_2 sequestration rate and total amount, and (b) two-phase fraction under different injection temperatures.

temperature reservoir has a strong thermal buffering capacity, and that the localized thermal disturbance induced by variations in injection temperature is insufficient to macroscopically alter the overall performance of hydrate-based CO_2 sequestration. This indicates that the sequestration performance is relatively insensitive to moderate injection-temperature variations within the investigated range, providing operational flexibility for injection-temperature control.

The present sensitivity analysis was limited to the investigated injection-temperature range. The effects of salinity were not incorporated into the current model, while the influences of well placement and well spacing were not systematically evaluated. These factors may affect CO_2 migration and hydrate formation and should be considered in future studies to further improve the robustness and applicability of the proposed modeling framework.

3.2. *CO_2 storage and reservoir deformation behavior in a two-well injection system*

3.2.1. *Long-term storage performance*

Based on the preceding analysis, a dual-well model was established to examine CO_2 storage performance under a two-well configuration. Given that the CO_2 diffusion width in the single-well system after 5000 days was approximately 60 m, the two wells were placed laterally with a spacing of 50 m to better represent fluid interaction within the reservoir. Fig. 20 presents the distributions of key physical fields in the reservoir during dual vertical-well injection. As injection continued over time, hydrate cap layers formed above each well. By the end of the storage period, the hydrate layers between the two wells had merged, creating a continuous barrier that helps prevent CO_2 leakage through the inter-well region. Figs. 20c and d shows that the dual-well system altered pressure distribution as well as heat and mass transfer processes, leading to a broader CO_2 diffusion area. Furthermore, the well configuration

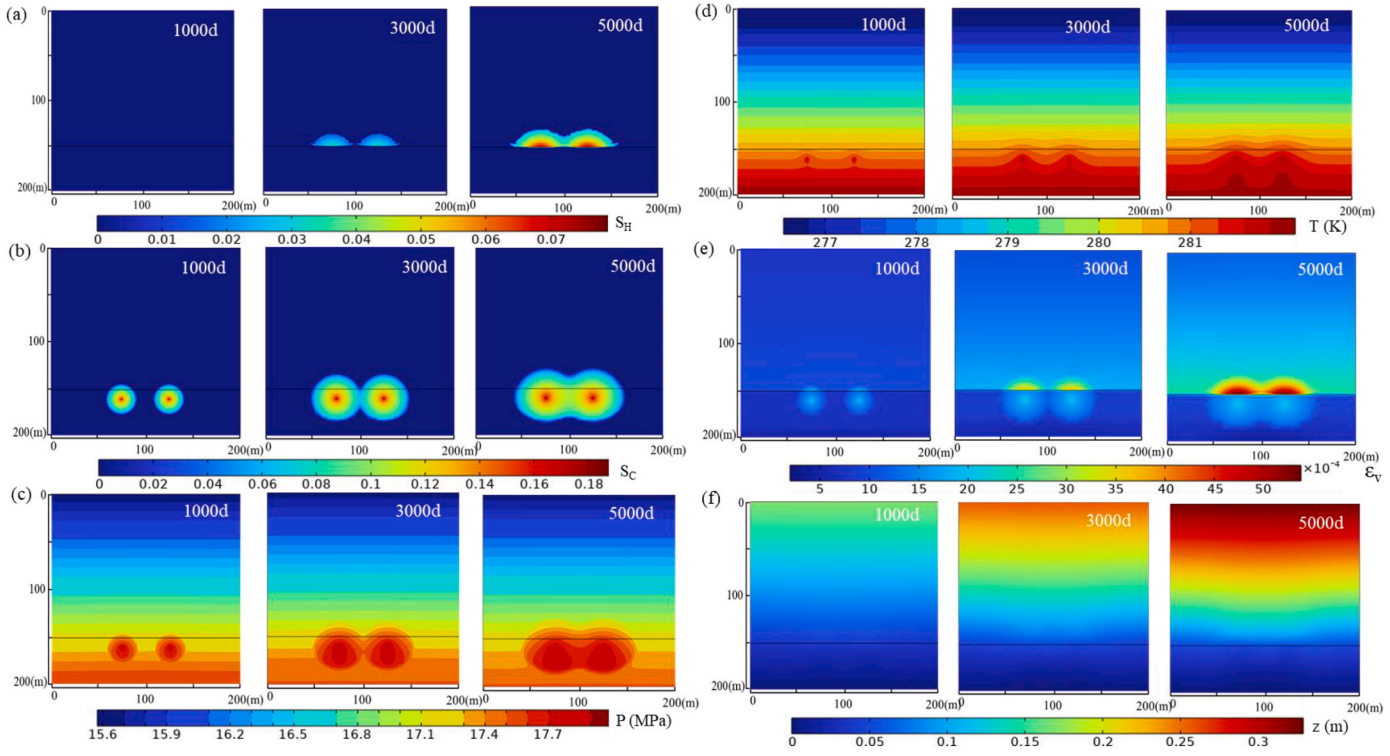


Fig. 20. Spatial distribution after 5000 days of dual vertical well injection: (a) hydrate saturation, (b) CO_2 saturation, (c) pressure, (d) temperature, (e) volumetric strain, and (f) displacement.

influenced formation mechanical behavior by modifying these transport processes and the resulting hydrate distribution. In the dual-well system, the extent of formation strain increased, and reservoir displacement exhibited more pronounced variation.

3.2.2. Analysis of reservoir deformation and stability

Fig. 21 presents the evolution of effective stress in the reservoir during CO_2 hydrate storage under a dual-well system, with injection wells located at (75, −160) and (125, −160). The results show that effective stress generally increased with depth. At the interface between the two reservoir layers, CO_2 diffusion and hydrate formation raised pore pressure, inducing notable disturbance in the principal stress field. Fig. 21b further illustrates the distribution of horizontal effective principal stress. Near the base of the hydrate formation zone, upward-migrating CO_2 formed hydrates and reduced pore pressure, which increased the effective principal stress around both well locations, reaching a maximum value of 2.86 MPa. Compared with the single-well system, however, stress variation on this plane was less pronounced. This likely occurred because, in the dual-well configuration, injected CO_2 diffused laterally between the wells, promoting a more uniform stress distribution. Consequently, stress concentration near individual wells was alleviated, and overall stress variability in the dual-well system became relatively lower. To further assess mechanical stability, the effective principal stress paths and the critical line defined by the Mohr-Coulomb failure criterion were analyzed. The results indicate that injection for 5000 days under the dual-well system did not induce formation failure.

Fig. 22 shows the reservoir displacement during CO_2 injection in the dual-well system, including both vertical (Fig. 22a) and horizontal (Fig. 22b) displacement distributions along the injection profile. The results indicate that in-plane displacement was consistently higher than in the single-well system. Specifically, displacement at the base of the hydrate formation zone increased by 0.03 m, and seafloor displacement increased by 0.13 m. Since a greater volume of CO_2 was injected and the wells were arranged laterally, the reservoir experienced stronger mechanical disturbance, leading to larger in-plane displacement and a broader range of displacement variation.

3.3. Comparison of CO_2 storage performance between single-well and dual-well systems

Fig. 23 presents a comparison of CO_2 storage performance between single-well and dual-well systems during CO_2 injection and hydrate formation in the subsea reservoir. To ensure a consistent comparison, the sequestration performance of the single-well and dual-well systems was first evaluated over the same injection period of 5000 days under identical total injection rates. The results show that both the storage rate and total CO_2 storage were significantly higher in the dual-well system than in the single-well system. The peak storage rate in the dual-well system was more than double that of the single-well case. The dual-well system increased the storage capacity by 2.48 times compared with the single-well system. This improvement can be attributed to the

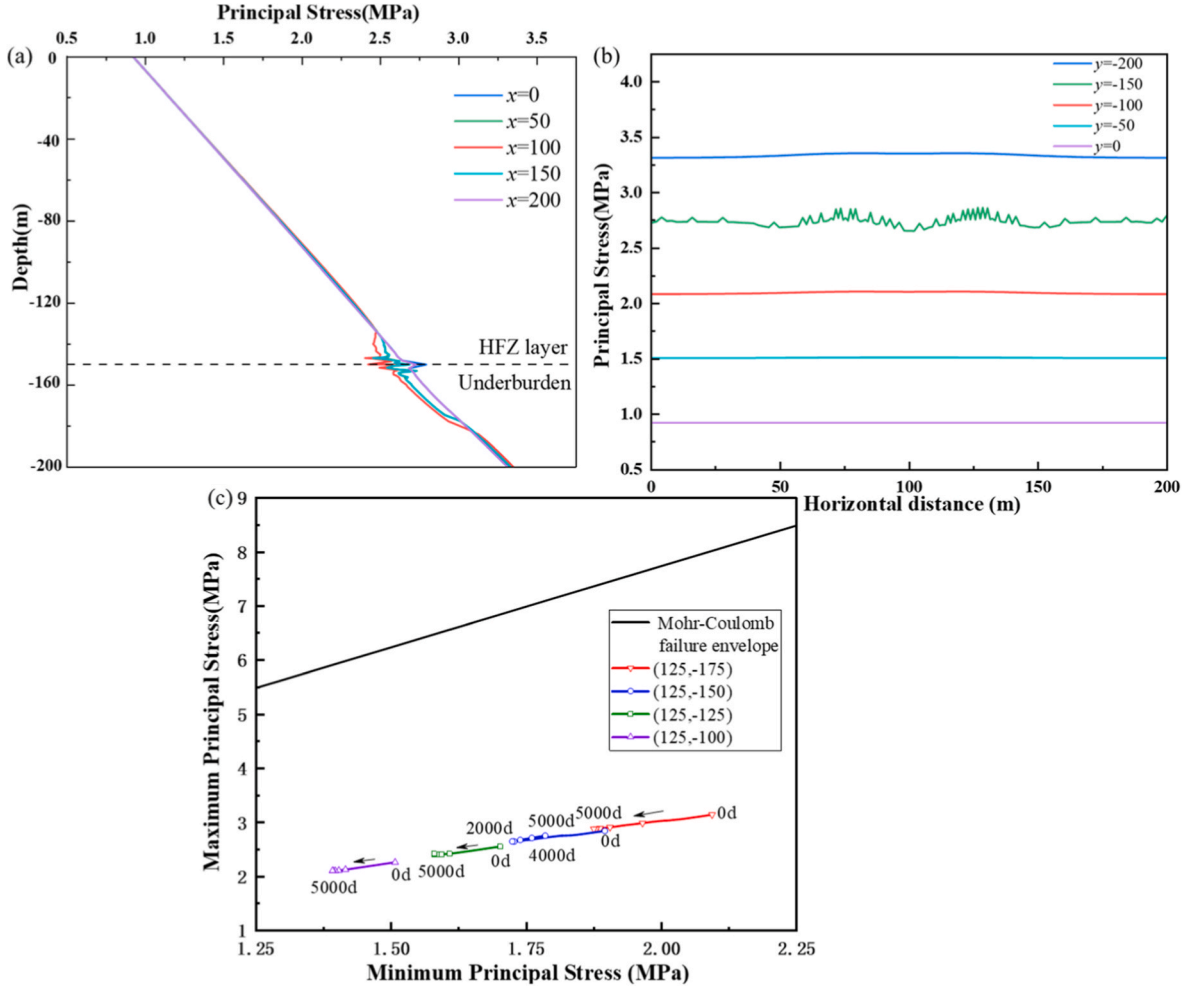


Fig. 21. Dual vertical well injection: variation of reservoir stress on different planes—(a) vertical stress and (b) horizontal stress versus distance, and (c) stress failure curves at monitoring points.

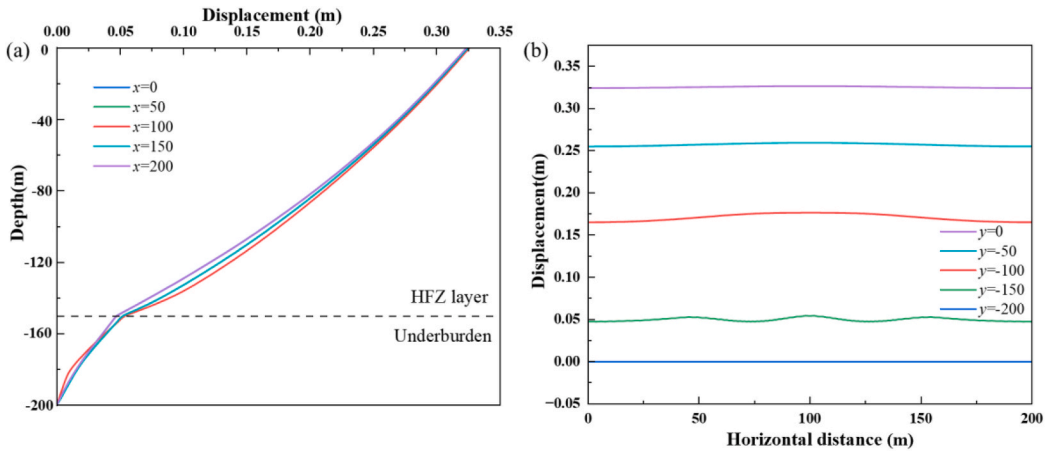


Fig. 22. Dual vertical well injection: variation of reservoir displacement on different planes—(a) vertical displacement and (b) horizontal displacement versus distance.

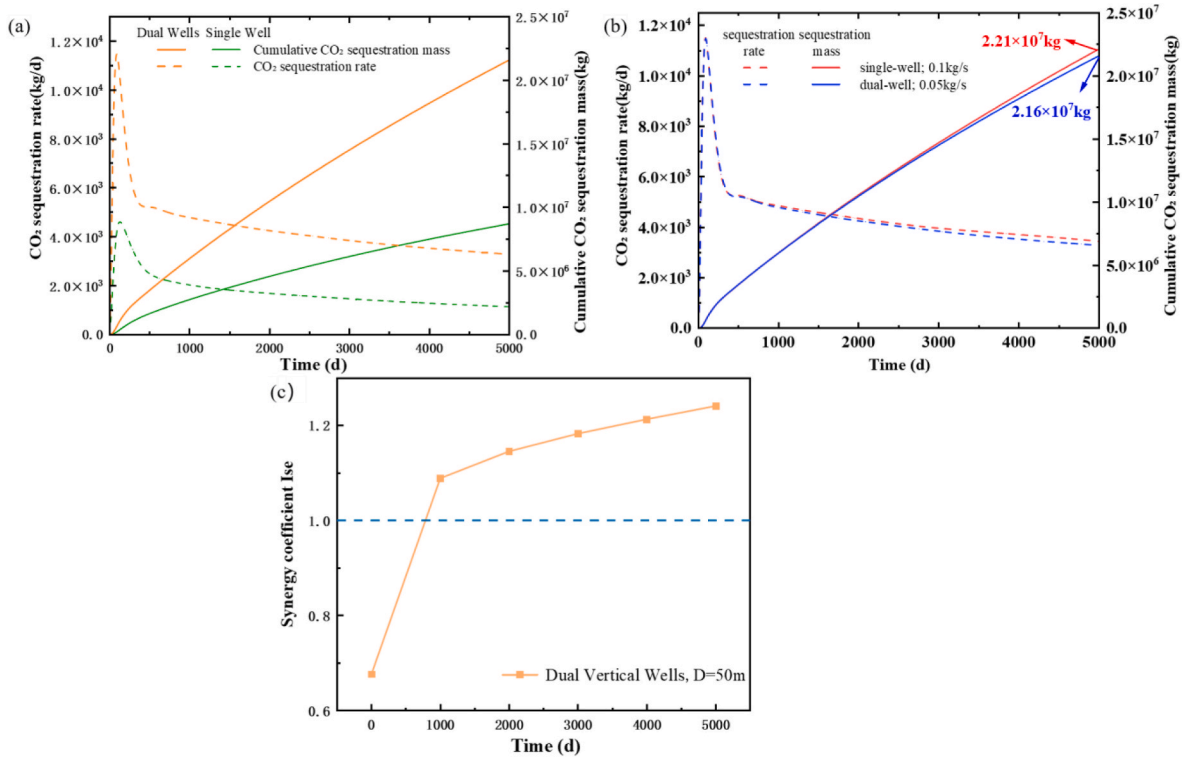


Fig. 23. CO_2 storage performance of single-well and dual-well injection systems: (a) storage rate and cumulative storage; (b) comparison between the single-well (0.1 kg/s) and dual-well (0.05 kg/s per well) cases; (c) synergy coefficient over time.

expansion of the pressure and CO_2 migration fields generated by the two wells, which promoted a wider spatial distribution of injected CO_2 and increased the effective sediment volume available for hydrate formation and CO_2 storage. The use of a dual-well configuration enhanced heat and mass transfer as well as multiphase flow, which promoted hydrate formation, expanded the CO_2 diffusion area, and ultimately improved storage efficiency. It should be noted that the total CO_2 injection rate in the dual-well system (2×0.05 kg/s) is equal to that in the single-well system (0.1 kg/s), resulting in similar sequestration-rate evolution (Fig. 23b). Nevertheless, the dual-well configuration slightly reduces the sequestration rate and cumulative sequestration capacity due to changes in the pressure field and hydrate distribution.

To quantify the synergistic effect between the two wells, a synergy coefficient I_{se} was calculated based on total CO_2 storage: $I_{se} = \frac{Q_{double}}{2 \cdot Q_{single}}$, where Q_{double} is the total CO_2 storage under dual-well injection, Q_{single} is the total CO_2 storage under single-well injection, and the factor 2 represents the number of wells. Fig. 23c illustrates the variation of the synergy coefficient with storage time. The coefficient increased over time, with values exceeding 1 after about 90 days. This indicates that the dual-well system enhanced CO_2 storage performance relative to two independent single wells. The improved performance of the dual-well system is not solely attributed to the increased number of injection wells. The interaction between the two wells expands the effective CO_2 migration region and modifies the pressure and flow fields. Meanwhile, hydrate formation and sediment deformation affect porosity and permeability evolution, collectively contributing to the enhanced storage performance of the dual-well system. However, the synergy coefficient is used here only to quantify the inter-well storage interaction and

should not be interpreted as a comprehensive indicator of the engineering feasibility of the dual-well strategy. The practical performance of the dual-well configuration should also be evaluated in conjunction with pressure and geomechanical responses.

In addition, to further compare the storage performance of single-well and dual-well systems, the final injection duration and total storage for both configurations were calculated, as presented in Fig. 24. The single-well system achieved a total storage of 1.14×10^7 kg over 9110 days, whereas the dual-well system stored 4.04×10^7 kg over 12345 days. Compared to the single-well system, the dual-well configuration expanded the drainage area and modified the internal reservoir structure, thereby enhancing flow capacity and allowing CO_2 injection to continue for a longer period. Simultaneously, fluid interactions between the wells promoted CO_2 migration and hydrate formation, leading to higher overall storage capacity. Fig. 24c further shows the final vertical displacement for the two systems. After 9110 days, the single-well system reached a maximum displacement of 0.27 m, while the dual-well system attained 0.48 m after 12345 days. Although the dual-well system extended the injection period, the increase in displacement was less than double that of the single-well case. This indicates that the dual-well system can prolong injection time without proportionally increasing reservoir displacement.

4. Conclusions

This study developed a fully coupled thermal–hydraulic–mechanical–chemical (THMC) model to simulate CO_2 hydrate storage and applied it to the Shenhu reservoir in the South China Sea. By incorporating the coupling between mechanical deformation, CO_2 injection, and hydrate formation, the storage performance and reservoir stability of subsea CO_2 hydrate sequestration were evaluated. The evolution of key physical fields in the reservoir was analyzed, and a dual-well injection strategy was proposed. The main conclusions are as follows:

(1) CO_2 hydrate storage effectively enables long-term carbon sequestration. After 5000 days of injection, the total stored CO_2 reached 8.69×10^6 kg, of which 27% was retained in the hydrate phase. The resulting hydrate cap exhibited a lateral extent of about 50 m, providing effective sealing, and the storage system demonstrated long-term stability overall.

(2) Injection rate significantly influences storage performance and safety. Following the start of CO_2 injection, effective stress near the well declined rapidly, inducing detectable subsidence at the base of the hydrate formation zone and at the seafloor (up to 0.02 m and 0.2 m, respectively). Over the 5000 days period, the principal effective stress did not evolve toward the yield-failure envelope. Appropriately increasing the injection rate can raise both the storage rate and total CO_2 stored. For example, when the injection rate was increased from 0.01 kg/s to 0.1 kg/s, total CO_2 storage grew by 22.7 times, while the hydrate-phase fraction decreased from 29% to 26%. Consequently, excessively high injection rates may induce stress disturbance in the formation, and injection strategies should be dynamically optimized based on site-specific geological conditions.

(3) Reservoir deformation influences heat and mass transfer, ultimately reducing hydrate formation and CO_2 storage. Relative to the thermal–hydraulic–chemical (THC) three-field coupled model, omitting mechanical effects underestimated the reduction in porosity and permeability, leading to an overestimation of CO_2 storage (predicted increase from 8.69×10^6 kg to 8.82×10^6 kg). After incorporating deformation via the THMC model, the resulting permeability was approximately 13.53% lower than that predicted by the THC model. The hydrate formation range became more concentrated near the well bottom, resulting in an overall reduction in CO_2 storage of about 1.42% and a decrease in hydrate formation of 2.04%. This indicates that reservoir deformation restricts injection-driven transport pathways while simultaneously enhancing local sealing capacity.

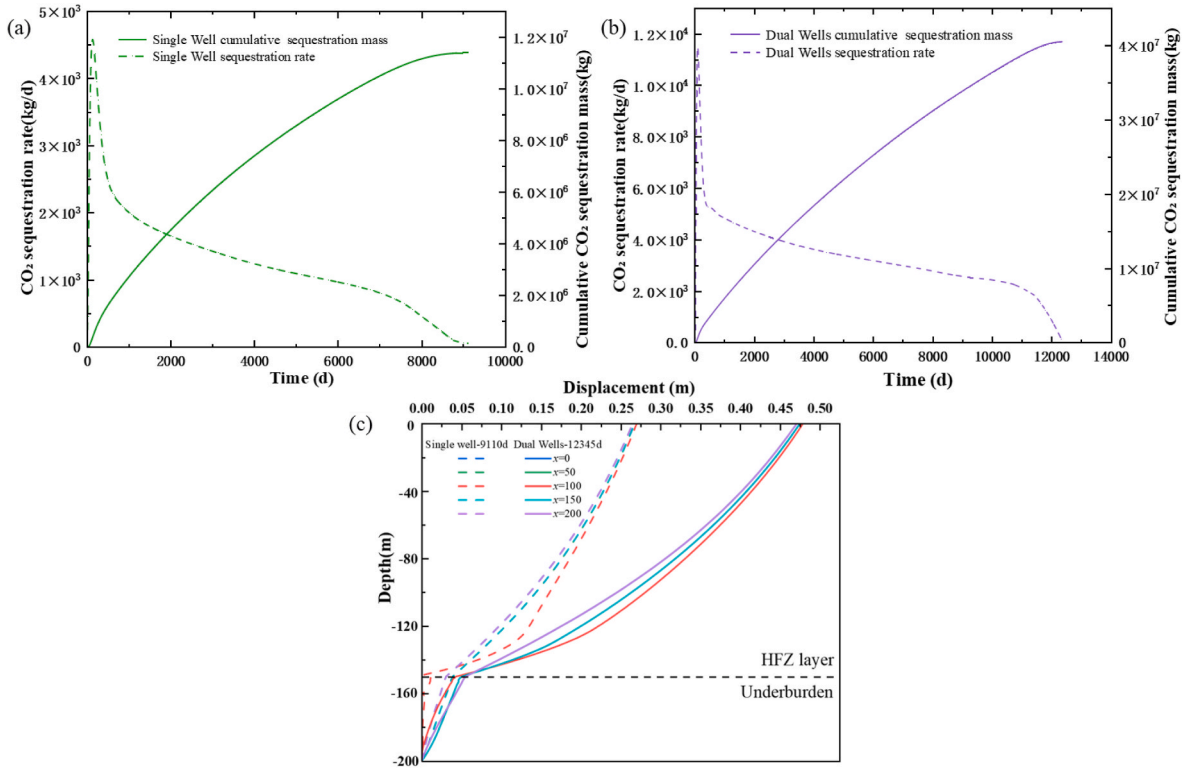


Fig. 24. Comparison of CO_2 final storage rate and total storage: (a) single-well system, (b) dual-well system; (c) comparison of final vertical displacement between single-well and dual-well systems.

(4) The dual-well system substantially improved storage performance through a synergistic inter-well effect. It expanded the CO_2 diffusion range and enhanced heat and mass transfer as well as multiphase flow, ultimately increasing final CO_2 storage by a factor of 2.48 compared with the single-well system. In addition, the dual-well configuration enabled longer injection duration and provided greater overall storage capacity.

CRediT authorship contribution statement

Hui Yang: Writing – original draft, Formal analysis, Conceptualization. **Shuanshi Fan:** Validation, Supervision. **Xuemei Lang:** Project administration, Funding acquisition. **Chenlu Xu:** Validation. **Yanhong Wang:** Writing – review & editing, Supervision, Formal analysis. **Mengyang Li:** Methodology, Data curation.

Declaration of competing interest

The authors declare the following financial interests/personal relationships which may be considered as potential competing interests: Xuemei Lang reports financial support was provided by the Special Project for Marine Economy Development of Guangdong. If there are other authors, they declare that they have no known competing financial interests or personal relationships that could have appeared to influence the work reported in this paper.

Acknowledgments

This work was supported by the Special Project for Marine Economy Development of Guangdong (six marine industries) (GDNRC[2024]33).

Appendix A. Supplementary data

Supplementary data to this article can be found online at https://doi.org/10.1016/j.geoen.2026.214877.

Data availability

Data will be made available on request.

References

Allen, M.R., Frame, D.J., Huntingford, C., Jones, C.D., Lowe, J.A., Meinshausen, M., Meinshausen, N., 2009. Warming caused by cumulative carbon emissions towards the trillionth tonne. Nature 458, 1163–1166.
Aminnaji, M., Qureshi, M.F., Dashti, H., Hase, A., Mosalanejad, A., Jahanbakhsh, A., Babaei, M., Amiri, A., Maroto-Valer, M., 2024. CO2 gas hydrate for carbon capture and storage applications – part 2. Energy 300, 131580.
Anderson, G.K., 2003. Enthalpy of dissociation and hydration number of carbon dioxide hydrate from the Clapeyron equation. J. Chem. Therm. 35, 1171–1183.
Bahmaee, A., Masuda, Y., Murata, S., 2024. Numerical modelling of CO2-in-water emulsion injection into a water-saturated core. Gas Sci. Eng. 131, 205485.
Cheng, F., Sun, X., Li, Y., Ju, X., Yang, Y., Liu, X., Liu, W., Yang, M., Song, Y., 2023. Numerical analysis of coupled thermal-hydro-chemo-mechanical (THCM) behavior to joint production of marine gas hydrate and shallow gas. Energy 281, 128224.
Cheng, Y., Li, L., Yuan, Z., Wu, L., Mahmood, S., 2013. Finite element simulation for fluid–solid coupling effect on depressurization-induced gas production from gas hydrate reservoirs. J. Nat. Gas Sci. Eng. 10, 1–7.
Cui, G., Wang, Y., Rui, Z., Chen, B., Ren, S., Zhang, L., 2018. Assessing the combined influence of fluid-rock interactions on reservoir properties and injectivity during CO2 storage in saline aquifers. Energy 155, 281–296.
Dhamu, V., Qureshi, M.F., Abubakar, S., Usadi, A., Barckholtz, T.A., Mhadeshwar, A.B., Linga, P., 2023. Investigating high-pressure liquid CO2Hydrate formation, dissociation kinetics, and morphology in brine and freshwater static systems. Energy Fuels 37, 8406–8420.
Fahed Qureshi, M., Zheng, J., Khandelwal, H., Venkataraman, P., Usadi, A., Barckholtz, T.A., Mhadeshwar, A.B., Linga, P., 2022. Laboratory demonstration of the stability of CO2 hydrates in deep-oceanic sediments. Chem. Eng. J. 432, 134290.
Gu, Y., Liu, X., Li, Y., Lu, H., Xu, C., Ren, J., Chen, G., Linga, P., Zhao, J., Yin, Z., 2025. Feasibility analysis of liquid CO2 injection and sequestration as hydrates in South China Sea marine sediments over 100 years. Appl. Energy 380, 125068.
Hepburn, C., Adlen, E., Beddington, J., Carter, E.A., Fuss, S., Mac Dowell, N., Minx, J.C., Smith, P., Williams, C.K., 2019. The technological and economic prospects for CO2 utilization and removal. Nature 575, 87–97.
Inoue, Y., Ohgaki, K., Hirata, Y., Kunugita, E., 1996. Numerical study on effects of hydrate formation on deep sea CO_2 storage. J. Chem. Eng. Jpn. 29, 648–655.
Jafari, A., Vahab, M., Broumand, P., Khalili, N., 2023. An eXtended finite element method implementation in COMSOL multiphysics: thermo-hydro-mechanical modeling of fluid flow in discontinuous porous media. Comput. Geotech. 159, 105458.
Jeenmuang, K., Pornaroontham, P., Fahed Qureshi, M., Linga, P., Rangsunvigit, P., 2024. Micro kinetic analysis of the CO2 hydrate formation and dissociation with L-tryptophan in brine via high pressure in situ Raman spectroscopy for CO2 sequestration. Chem. Eng. J. 479, 147691.
Juanes, R., Spiteri, E.J., Orr Jr., F.M., Blunt, M.J., 2006. Impact of relative permeability hysteresis on geological CO2 storage. Water Resour. Res. 42.
Khoramian, R., Issakhov, M., Pourafshary, P., Aidarova, S., Sharipova, A., 2026c. Reactive transport modeling of CO2 trapping in carbonate saline aquifers: coupled effects of wettability, temperature, and salinity on mineralization and storage efficiency. Fuel 406, 137038.
Khoramian, R., Nurmyrza, M., Lee, W., 2025a. Influence of oil-wet wettability and nanoparticle treatments on carbonate rock dissolution and CO2 leakage risk in saline aquifers. Energy Fuels 39, 20489–20505.
Khoramian, R., Salaudeen, I., Pourafshary, P., Riazi, M., Kharrat, R., 2025b. Wettability-driven variations in CO2 trapping: coupled impact of capillary forces and reactive transport in saline aquifers. In: SPE Annual Caspian Technical Conference and Exhibition.
Khoramian, R., Salaudeen, I., Pourafshary, P., Riazi, M., Kharrat, R., 2026a. Beyond wettability: flow regime and geological heterogeneity controls on CO2 trapping efficiency and dissolution behavior in saline aquifers. J. Clean. Prod. 543, 147584.
Khoramian, R., Salaudeen, I., Pourafshary, P., Riazi, M., Kharrat, R., 2026b. Impact of wettability on CO2 mineral trapping in carbonate saline aquifers: a reactive transport simulation study. Greenhouse Gases Sci. Technol. 16, 46–61.
Koide, H., Takahashi, M., Shindo, Y., Tazaki, Y., Iijima, M., Ito, K., Kimura, N., Omata, K., 1997. Hydrate formation in sediments in the sub-seabed disposal of CO2. Energy 22, 279–283.
Li, M., Fan, S., Wang, Y., Lang, X., Li, G., 2025b. Optimizing CO2 hydrate storage and avoiding leakage: numerical analysis of the self-restoring formation process of hydrate caps in submarine sandy silts. Mar. Petrol. Geol. 179, 107450.
Li, Y., Zhang, T., Yuan, L., Tang, M., Li, R., Chen, Y., Luo, W., Zhang, C., 2025a. CO2 hydrate sequestration in unsealed submarine sediments: a 4D pore-scale experimental investigation. Gas Sci. Eng. 143, 205734.
Liu, X., Zhang, J., Gu, Y., Huang, H., Li, Y., Sun, J., Lu, H., Xu, C., Ren, J., Yin, Z., 2025. Investigation on liquid CO2 forming CO2 hydrates in sands: a kinetic study with implication on hydrate-based CO2 sequestration. Chem. Eng. J. 505, 159179.
Liu, Z., Xu, J., Li, H., Li, S., Fan, X., 2023. Numerical investigation of CO2 storage capacity via hydrate in deep-sea sediments. Energy Fuels 37, 18996–19010.
Ning, F., Yu, Y., Kjelstrup, S., Vlugt, T.J.H., Glavatskiy, K., 2012. Mechanical properties of clathrate hydrates: status and perspectives. Energy Environ. Sci. 5, 6779–6795.
Pandey, G., Poothia, T., Kumar, A., 2022. Hydrate based carbon capture and sequestration (HBCCS): an innovative approach towards decarbonization. Appl. Energy 326, 119900.
Rehman, A.N., Bavoh, C.B., Pendyala, R., Lal, B., 2021. Research advances, maturation, and challenges of hydrate-based CO2 sequestration in porous media. ACS Sustain. Chem. Eng. 9, 15075–15108.
Rochelle, C.A., Camps, A.P., Long, D., Milodowski, A., Bateman, K., Gunn, D., Jackson, P., Lovell, M.A., Rees, J., Long, D., Lovell, M.A., Rees, J.G., Rochelle, C.A., 2009. Can CO2 hydrate assist in the underground storage of carbon dioxide?. In: Sediment-Hosted Gas Hydrates: New Insights on Natural and Synthetic Systems. Geological Society of London.
Rutqvist, J., Moridis, G.J., Grover, T., Silpngarmlert, S., Collett, T.S., Holdich, S.A., 2012. Coupled multiphase fluid flow and wellbore stability analysis associated with gas production from Oceanic hydrate-bearing sediments. J. Petrol. Sci. Eng. 92–93, 65–81.
Salaudeen, I., Khoramian, R., Riazi, M., Pourafshary, P., Cortés, F.B., 2026. Prolong impact of temperature on CO2 dissolution in finite heterogeneous saline aquifers. Energy Fuels 40, 2075–2090.
Sarkar, S., Singh, I.V., Mishra, B.K., 2022. A simple and efficient implementation of localizing gradient damage method in COMSOL for fracture simulation. Eng. Fract. Mech. 269, 108552.
Sinehbaghizadeh, S., Saptoro, A., Mohammadi, A.H., 2022. CO2 hydrate properties and applications: a state of the art. Prog. Energy Combust. Sci. 93, 101026.
Singh, R.P., Shekhawat, K.S., Das, M.K., Muralidhar, K., 2020. Geological sequestration of CO2 in a water-bearing reservoir in hydrate-forming conditions. Oil Gas Sci. Technol. – Rev. IFP Energies nouvelles 75, 51.
Sun, H., Chen, J., Ji, X., Karunakaran, G., Chen, B., Ranjith, P.G., Song, Y., Yang, M., 2024. Optimizing CO2 hydrate storage: dynamics and stability of hydrate caps in submarine sediments. Appl. Energy 376, 124309.
Sun, J., Zhang, L., Ning, F., Lei, H., Liu, T., Hu, G., Lu, H., Lu, J., Liu, C., Jiang, G., Liang, J., Wu, N., 2017. Production potential and stability of hydrate-bearing sediments at the site GMGS3-W19 in the South China Sea: a preliminary feasibility study. Mar. Petrol. Geol. 86, 447–473.
Sun, X., Luo, H., Soga, K., 2018. A coupled thermal–hydraulic–mechanical–chemical (THMC) model for methane hydrate bearing sediments using COMSOL multiphysics. J. Zhejiang Univ. - Sci. 19, 600–623.
Teng, Y., Zhang, D., 2018. Long-term viability of carbon sequestration in deep-sea sediments. Sci. Adv. 4, eaao6588.

Wan, Y., Wu, N., Hu, G., Xin, X., Jin, G., Liu, C., Chen, Q., 2018. Reservoir stability in the process of natural gas hydrate production by depressurization in the shenhu area of the South China Sea. Nat. Gas Ind. B 5, 631–643.
Wang, F., Shen, K., Zhang, Z., Zhang, D., Wang, Z., Wang, Z., 2023a. Numerical simulation of natural gas hydrate development with radial horizontal wells based on thermo-hydro-chemistry coupling. Energy 272, 127098.
Wang, J., Zhang, L., Ge, K., Dong, H., 2021. Capillary pressure in the anisotropy of sediments with hydrate formation. Fuel 289, 119938.
Wang, K., Ma, L., Taylor, K.G., 2023b. Microstructure changes as a response to CO2 storage in sedimentary rocks: recent developments and future challenges. Fuel 333, 126403.
Wang, P., Li, Y., Sun, N., Han, S., Wang, X., Su, Q., Li, Y., He, J., Yu, X., Du, S., Francisco, J.S., Zhu, J., Zhao, Y., 2024a. Hydrate technologies for CO2 capture and sequestration: status and perspectives. Chem. Rev. 124, 10363–10385.
Wang, T., Fan, Z., Sun, L., Yang, L., Zhao, J., Zhang, L., Song, Y., 2024b. Evaluation of stratigraphic adaptability for hydrate-based CO2 sequestration in marine clay-containing reservoirs. Chem. Eng. J. 501, 157711.
Wei, R., Xia, Y., Wang, Z., Li, Q., Lv, X., Leng, S., Zhang, L., Zhang, Y., Xiao, B., Yang, S., Yang, L., Zhao, J., Song, Y., 2022. Long-term numerical simulation of a joint production of gas hydrate and underlying shallow gas through dual horizontal wells in the South China Sea. Appl. Energy 320, 119235.
Wu, P., Li, Y., Liu, W., Liu, Y., Wang, D., Song, Y., 2020a. Microstructure evolution of hydrate-bearing sands during thermal dissociation and ensued impacts on the mechanical and seepage characteristics. J. Geophys. Res. Solid Earth 125, e2019JB019103.
Wu, P., Li, Y., Liu, W., Sun, X., Kong, X., Song, Y., 2020b. Cementation failure behavior of consolidated gas hydrate-bearing sand. J. Geophys. Res. Solid Earth 125, e2019JB018623.
Xia, Y., Gao, P., Jiang, Z., Fan, Q., Wei, R., Li, Q., Zhang, L., Yu, T., Zhao, J., Yang, L., Song, Y., 2024. Numerical simulation of CO2 storage in subseabed sediments in the shenhu area, South China Sea: the effect of Reservoir permeability anisotropy. Energy Fuels 38, 14.
Xia, Y., Yu, T., Yang, L., Chen, B., Jiang, L., Yang, M., Song, Y., 2025. Multi-state CO2 distribution patterns for subsea carbon sequestration assisted by large-scale CO2 hydrate caps. Energy 320, 135231.
Yang, M., Wu, M., Yang, Z., Wang, P., Chen, B., Song, Y., 2024. Behaviors of hydrate cap formation via CO2-H2O collaborative injection:applying to secure marine carbon storage. Gas Sci. Eng. 131, 205451.
Yin, F., Gao, Y., Chen, Y., Sun, B., Li, S., Zhao, D., 2022b. Numerical investigation on the long-term production behavior of horizontal well at the gas hydrate production site in South China Sea. Appl. Energy 311, 118603.
Yin, F., Gao, Y., Zhang, H., Sun, B., Chen, Y., Gao, D., Zhao, X., 2022a. Comprehensive evaluation of gas production efficiency and reservoir stability of horizontal well with different depressurization methods in low permeability hydrate reservoir. Energy 239, 122422.
Yu, T., Sato, T., Nakashima, T., Inui, M., Oyama, H., 2016. An integrated model for CO2 hydrate formation in sand sediments for sub-seabed CO2 storage. Int. J. Greenh. Gas Control 52, 250–269.
Zhang, Z., Li, Y., Xie, Z., Li, S., He, J., Li, X., Lu, C., Qin, X., 2024. Optimizing CO2 hydrate sequestration in subsea sediments through cold seawater pre-injection. Sustainability 16, 8548.
Zhao, G., Yang, M., Pang, W., Gong, G., Zheng, J.-n., Zhang, P., Chen, B., 2022. Effects of hydrate cap on leakage prevention and capacity improvement of sub-seabed CO2 sequestration. Chem. Eng. J. 450, 138493.
Zheng, J., Chong, Z.R., Qureshi, M.F., Linga, P., 2020. Carbon dioxide sequestration via gas hydrates: a potential pathway toward decarbonization. Energy Fuels 34, 10529–10546.
Zhou, M., Soga, K., Yamamoto, K., 2020. Upscaling techniques for fully coupled THM simulation and application to hydrate gas production tests. Comput. Geotech. 124, 103596.